nature communications

Article

https://doi.org/10.1038/s41467-025-67209-2

A recurrent pathogenic *BRCA2* truncating variant reveals a role for BRCA2-PCAF complex in modulating NF-κB-driven transcription

Received: 29 April 2025

Accepted: 24 November 2025

Published online: 10 December 2025

Check for updates

Anna Minello[1,2,16], Jesus Gomez-Escudero[3,16], Sreerama Chaitanya Sridhara[3,16], Charlotte Martin[1,2], Elodie Girard[4], Juan C. Cañas[3], Yasin Memari[5,6], Maria Rose Bustos[7,8], Antonio Galarreta[9], Virginie Boucherit[1,2], Evgeny Imyanitov[10], Sigridur Klara Bodvarsdottir[8], Sylvain Baulande[11], Anne Vincent-Salomon[12], Nicolas Servant[4], Matthias Altmeyer[9], Stefan Sigurdsson[7,8], Dominique Stoppa-Lyonnet[13,14,15], Serena Nik-Zainal[5,6] & Aura Carreira[1,2,3]

Germline monoallelic truncating mutations in BRCA2, a key mediator of homologous recombination (HR), predispose individuals to breast and ovarian cancer. Tumorigenesis is typically attributed to biallelic inactivation, yet evidence suggests haploinsufficiency can suffice in some contexts. We model two pathogenic BRCA2 truncating variants in heterozygosis in non-tumorigenic breast epithelial cells. One variant is not expressed and confers PARP inhibitor (PARPi) sensitivity and reduced HR, indicating haploinsufficiency. In contrast, the other produces a truncated protein that rewires transcription in cells and tumors. Mechanistically, this truncated product acts as a dominant negative by forming abnormal oligomers with full-length BRCA2 and sequestering the PCAF acetyltransferase. This interaction reduces global histone H4 acetylation and suppresses NF-κB transcriptional activity, ultimately altering epithelial migration. Our findings reveal a BRCA2–PCAF axis that modulates NF-κB signaling, a process co-opted by a recurrent BRCA2 pathogenic variant.

Inactivating germline mutations affecting a single copy of *BRCA2* are associated with an increased risk of breast and ovarian cancer. However, the precise sequence of events that takes place from the inherited *BRCA2* mono-allelic mutation to tumorigenesis remains poorly defined. A wealth of evidence suggests that BRCA2 exerts its tumor-suppressive activity through its role in DNA repair by homologous recombination (HR)[1]. At DNA double-strand breaks (DSBs) or replicative DNA lesions, BRCA2 binds and loads RAD51 onto the resected

[1]Institut Curie, Université PSL CNRS UMR3348, Orsay, France. [2]Université Paris-Saclay CNRS UMR3348, Orsay, France. [3]Genome Instability and Cancer Predisposition Laboratory, Centro de Biologia Molecular Severo Ochoa (CBM), CSIC-UAM, Madrid, Spain. [4]CBIO-Centre for Computational Biology, INSERM U900, Mines ParisTech, Paris, France. [5]Academic Department of Medical Genetics, School of Clinical Medicine, University of Cambridge, Cambridge, UK. [6]Early Cancer Institute, University of Cambridge, Cambridge, UK. [7]Cancer Research Laboratory, Faculty of Medicine, School of Health Sciences, University of Iceland, Reykjavik, Iceland. [8]BioMedical Center, School of Health Sciences, University of Iceland, Reykjavik, Iceland. [9]Department of Molecular Mechanisms of Disease, University of Zurich, Zurich, Switzerland. [10]N.N. Petrov National Medical Research Center of Oncology, Saint Petersburg, Russia. [11]Institut Curie, PSL University, ICGex Next-Generation Sequencing Platform, Paris, France. [12]Diagnostic and Theragnostic Medicine Division, Institut Curie, Paris, France, Institut Curie, Paris, France. [13]Department of Genetics, Institut Curie, Paris, France. [14]Paris-Cité University, Paris, France. [15]INSERM U830 Institut Curie, Paris, France. [16]These authors contributed equally: Anna Minello, Jesus Gomez-Escudero, Sreerama Chaitanya Sridhara. e-mail: acarreira@cbm.csic.es

ssDNA to promote pairing and strand exchange with the sister chromatid template for high-fidelity repair. At DSBs occurring at highly transcribed regions, BRCA2 supports DDX5-mediated unwinding of DNA-RNA hybrids for HR repair[2]. BRCA2 also protects stalled replication forks from aberrant nuclease degradation[3,4], and it prevents and promotes the repair of replication stress-associated ssDNA gaps via HR[5–8]. Other less canonical functions include a scaffolding role in cytokinesis[9,10], stabilizing kinetochore-microtubule attachments for proper chromosome segregation[11], and a poorly characterized transactivation function for transcription associated with the histone acetyltransferase P300/CBP-associated factor (PCAF), also known as KAT2B[12]. Whether these functions are linked to its tumor suppressor activity is still unclear.

As a tumor suppressor, the inactivation of the wild-type allele is believed to drive tumor formation; however, this event is not always found in BRCA2-associated tumors[13–17], suggesting that the mutated allele per se may trigger tumorigenesis. This idea entails an impact of the mutated allele in heterozygosis, which has been reported in different model systems, although with variable outcomes[1,18–28]. Interestingly, it has been reported that depending on the location of the variant in the sequence, the predisposition to breast or ovarian cancer is different[29] suggesting that, for example, depending on whether the variant is recognized by the nonsense-mediated mRNA decay machinery, the way tumorigenesis is triggered might differ. However, earlier studies found no evidence for this[30]. Here, to shed light on this question and the early steps of tumorigenesis, we recreated two well-known BRCA2 pathogenic truncating variants, c.771_775del (also known as 999del5, p.Asn257Lysfs*17, hereafter del5), or c.5946del (also known as 6174delT, p.Ser1982Argfs*22, hereafter delT) in heterozygosis in the non-malignant breast epithelial cell line MCF10A. We revealed that these two truncating variants lead to very different outcomes in heterozygosis: notably, cells carrying the del5 variant showed reduced levels of the BRCA2 full-length protein, high sensitivity to genotoxic stress, and reduced HR capacity. These results confirm haploinsufficiency. In contrast, cells carrying the delT variant showed normal levels of BRCA2, resistance to genotoxic stress, and normal HR capacity. Strikingly, the delT variant exerts a dominant-negative effect, inducing epigenetic and transcriptomic changes associated with epithelial cell proliferation and migration. These alterations were consistently observed in a small cohort of tumors harboring the same variant, but were absent in those expressing del5. In line with changes in proliferation and migration-related gene ontology (GO) terms, delT-expressing cells exhibited reduced proliferation and migration in 2D cultures, yet displayed enhanced invasive behavior in 3D matrices. Mechanistically, delT formed aberrant complexes with full-length BRCA2 and PCAF, a known BRCA2-interacting lysine acetyltransferase, resulting in decreased H4 acetylation and reduced phosphorylation of nuclear factor (NF-κB) p65—perturbations that likely drive the observed transcriptional reprogramming.

Collectively, our findings reveal a rewired BRCA2–PCAF–NF-κB axis that modulates cell migration and invasion in cells and tumors expressing the delT variant. Importantly, we demonstrate that BRCA2 truncating variants are not functionally equivalent: while del5 leads to haploinsufficiency, delT acts through a dominant-negative mechanism. Finally, the distinct chemotherapy responses observed in cells heterozygous for different variants highlight a potential avenue for stratified cancer prevention and treatment.[31,32]

Results

+/delT and +/del5 cells exhibit different sensitivity to PARPi and mitomycin C

To test haploinsufficiency associated with BRCA2, we chose to recreate two common germline pathogenic truncating variants identified in breast cancer patients: 1. c.5946delT or 6174delT (c.5946), a prevalent variant in individuals with an Ashkenazi Jewish ancestry[31–33] resulting in an early stop codon in exon 11 and a mislocalized truncated protein[34]. 2. 999del5 (c.771_775del), a founder mutation in Iceland responsible for ~70% of the *BRCA1/2* breast cancer predisposition in that population[35], resulting in a premature stop codon in exon 9. The corresponding truncated protein is unstable, not detected[36], and can be considered null.

Using transcription-activator-like effector nuclease (TALEn) and CRISPR-Cas9 methodology, we generated two independently derived cell lines bearing each mono-allelic truncating variant of BRCA2 in MCF10A, a non-transformed human mammary epithelial cell line[37] (Fig. 1a). The gene-edited population was sorted, the clones were expanded, and the mutation was verified by PCR amplification of the targeted genomic locus by Sanger sequencing (Fig. 1a, Supplementary Fig. 1a). For c.5946delT, the mutation obtained was c.5947delG (thereafter +/delT); however, given that it results in the same premature stop codon (at aa 2002), we decided to pursue our experiments with these cells. We also verified that no other mutations were present in the BRCA2 gene by WGS (Supplementary Fig. 1b).

Given the role of BRCA2 in maintaining genome stability, we evaluated the impact of the two pathogenic variants in heterozygosis in this function. We first determined the levels of BRCA2 protein in these cells. As expected, cells expressing +/del5 exhibited a reduction of BRCA2 protein levels to half compared to the MCF10A parental cells (Fig. 1b, Supplementary Fig. 1c). In contrast, +/delT cells showed similar BRCA2 protein levels to those of the MCF10A parental cells. Interestingly, a similar trend was observed for RAD51 (Fig. 1b, Supplementary Fig. 1c). This was despite similar levels of mRNA and protein of BRCA2 and RAD51 in the different clones expressing both variants (Supplementary Fig. 1d).

To evaluate the function of BRCA2 in these cells, we first used the PARP inhibitor Olaparib, a chemotherapeutic agent used in the clinic for HR-deficient *BRCA1/2*-mutated tumors[38,39]. As expected, cells depleted of BRCA2 showed high sensitivity to Olaparib whereas this was not the case for MCF10A cells (Fig. 1c). Remarkably, two +/del5 independent clones (Fig. 1a, Supplementary Fig. 1a) displayed increased sensitivity to PARPi (Fig. 1c), consistent with the reduced levels of BRCA2 and RAD51 observed in these cells (Fig. 1b, Supplementary Fig. 1c). Importantly, using gene-editing to correct del5 mutation to WT in clone #1 (Supplementary Fig. 1e) restored the resistance to levels comparable to that of the MCF10A parental cells (Fig. 1c) confirming that the sensitivity originated from the mutation in BRCA2. A similar trend was observed for the DNA crosslinking agent mitomycin C (MMC), +/del5 showing increased sensitivity at 4μM compared to MCF10A cells unlike the +/delT cells (Fig. 1d). Intriguingly, the resistance of +/delT was higher than that of the MCF10A cells in PARPi conditions, which when correcting the mutation (hereafter +/revdelT; Supplementary Fig. 1e) was restored to MCF10A levels (Supplementary Fig. 1f). +/delT cells also showed hyper-resistance to MMC treatment (Fig. 1d).

To get more insights into the dysfunction of +/del5 cells, we monitored the number of γH2AX foci, a well-established marker of DSBs, and RAD51 foci using quantitative imaging-based cytometry (QIBC) in cells treated either with MMC and PARPi or left untreated. In these settings, MMC (3 μM, 24 h) elicited a much stronger increase in DNA damage than PARPi (10 μM, 24 h) as manifested by the overall increased γH2AX foci in all cells (Supplementary Fig. 2a). Interestingly, +/delT cells showed decreased levels of γH2AX foci in MMC conditions (Supplementary Fig. 2a) correlating with its increased resistance to MMC in the MTT assay (Fig. 1d). Cells treated with Olaparib showed only a slight increase in γH2AX foci and RAD51 foci in all cells; however, in the presence of MMC, +/del5 and +/delT cells displayed a reduced number of RAD51 foci compared to the MCF10A parental cell line (Supplementary Fig. 2a).

As both Olaparib and MMC cause replicative lesions in addition to other types of DNA damage, we also tested cell sensitivity to nucleotide depletion by hydroxyurea (HU) treatment. In contrast to MMC and

https://doi.org/10.1038/s41467-025-67209-2

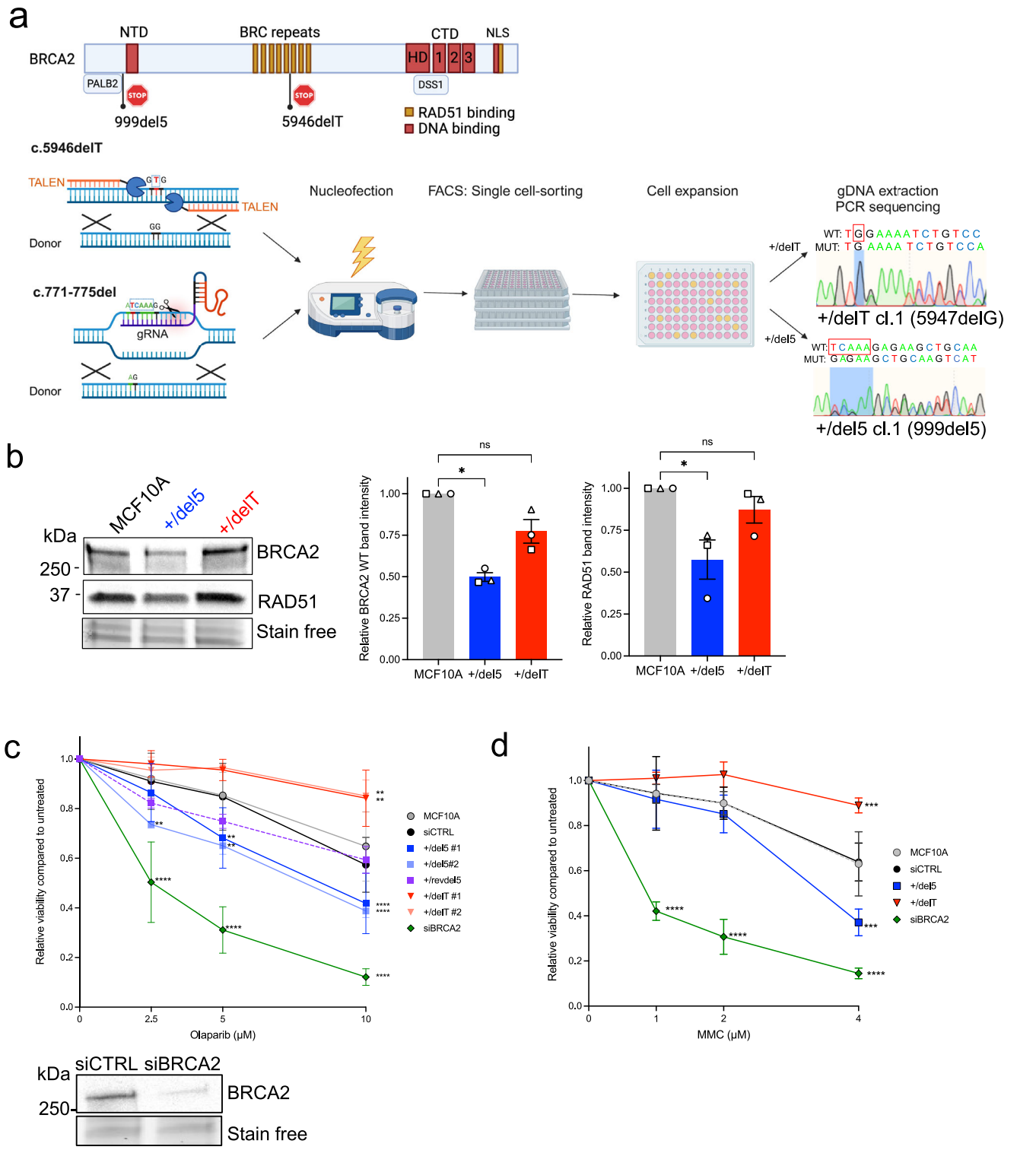

PARPi, neither clone showed sensitivity to HU, exhibiting comparable resistance to that of MCF10A cells (Supplementary Fig. 2b). Given that the HU elicited only mild sensitivity even at a high dose (5 mM) in these cells, we conducted clonogenic survival under the same conditions to confirm these results. Consistent with the MTT assay, the clonogenic survival assay showed the same outcome (Supplementary Fig. 2c), concluding that these cells do not display higher sensitivity to nucleotide depletion compared to the MCF10A controls.

Altogether, only +/del5 cells showed reduced protein levels of BRCA2 and RAD51 and exhibited increased sensitivity to PARPi and MMC, which was restored with the reverted mutation, whereas +/delT displayed increased resistance to both treatments. However, both cell lines moderately reduced the number of RAD51 foci in MMC conditions, whereas only +/delT cells showed a decreased number of γH2AX foci. Moreover, neither +/delT nor +/del5 cells changed sensitivity to nucleotide depletion-induced replication stress compared to the MCF10A controls.

+/del5 cells show reduced HR capacity and accumulate PARPi-induced ssDNA gaps

Given the sensitivity to different genotoxic agents, we directly measured the DSB repair capacity of +/del5 cells using a modified version

Fig. 1 | +/delT and +/del5 cells exhibit different sensitivity to PARPi and mitomycin C. a, Top: Schematic of BRCA2 protein structure showing functional domains and two truncating mutations (stop signs). DNA-binding domains (NTD, CTD) are shown in red; RAD51-binding domains in blue. Key interacting partners are indicated below. Abbreviations: NTD, N-terminal DNA-binding domain; CTD, C-terminal DNA-binding domain; HD, helical domain; OB folds, oligonucleotide/oligosaccharide-binding folds; NLS, nuclear localization signal. Figure created in BioRender.com. https://BioRender.com/y64b831 **Bottom left:** Workflow for generating stable heterozygous MCF10A cell lines using TALEN (Pacman icon) or CRISPR (scissors icon). **Bottom right:** Sanger sequencing confirming targeted mutations. **b** Representative Western blot showing BRCA2 (OP95 antibody) and RAD51 levels in the indicated cell lines. Quantification of BRCA2 and RAD51 normalized to stain-free loading control and MCF10A. Data represent mean ± SD from three independent experiments (symbols indicate replicates). Statistical analysis by the Kruskal–Wallis test followed by Dunn's multiple comparisons test. ns, not significant; *p = 0.0127 (BRCA2, MCF10A vs +/del5), *p = 0.0199 (RAD51, MCF10A vs +/del5). **c** Cell viability upon Olaparib treatment (6 days) in MCF10A, +/del5 (2 clones), +/delT (2 clones), +/revdel5, siBRCA2, and siCTRL cells. MTT assay data represent mean ± SD from: siCTRL and +/del5 (n = 6), MCF10A (n = 5), +/delT #1 and +/del5 #2 (n = 4), siBRCA2, +/delT #2, +/revdel5 (n = 3). Statistical analysis by the two-way ANOVA with Dunnett's multiple comparison; 2.5 μM (**p = 0.0087, MCF10A vs +/del5#2; ****p < 0.0001, MCF10A vs siBRCA2), 5 μM (**p = 0.0021, MCF10A vs +/del5#1; **p = 0.0033, MCF10A vs +/del5#2; ****p < 0.0001, MCF10A vs siBRCA2), 10 μM (****p < 0.0001, MCF10A vs +/del5#1; ****p < 0.0001, MCF10A vs +/del5#2; **p = 0.0055, MCF10A vs +/delT#1; **p = 0.0085, MCF10A vs +/delT#2; ****p < 0.0001, MCF10A vs siBRCA2). **d** Cell viability after 1 h MMC treatment at the indicated concentrations, measured on day 6. Data represent mean ± SD from three independent experiments. Statistical analysis by the two-way ANOVA with Dunnett's multiple comparison; 1.0 μM (****p < 0.0001, MCF10A vs siBRCA2), 2.0 μM (****p < 0.0001, MCF10A vs siBRCA2), 4.0 μM (***p = 0.0003, MCF10A vs +/del5#1; ***p = 0.0003, MCF10A vs +/delT#1; ****p < 0.0001, MCF10A vs siBRCA2). **Bottom left:** Western blot showing BRCA2 depletion (OP95 antibody) in siBRCA2 vs siCTRL cells before assays in **c**, **d**. Source data are provided as a Source Data file.

of our previous cell-based HR reporter assay[40]. This test measures DSB-mediated gene targeting activity at a specific locus (AAVS1 site) within the endogenous *PPP1R12C* gene. In this case, we co-transfected the cells with three plasmids, one expressing GFP-Cas9, one expressing a gRNA designed to cut at the AAVS1 site, and a promoter-less mCherry donor plasmid flanked by two homology sequences to the targeted locus. DSB-mediated gene targeting at the AAVS1 locus would result in mCherry expression from the endogenous PPP1R12C promoter, which is proportional to the HR repair capacity of the cells. Cells transfected with the mCherry plasmid and the GFP-Cas9, but without the gRNA, were used as controls. To enrich the population of transfected cells, we sorted the GFP-Cas9-positive cells 2 days after transfection. After 6 days in culture, 1.5% of MCF10A cells showed a mCherry-positive signal as compared to 0.3% of the control cells without gRNA. Similarly, 1.2% of +/delT cells expressed mCherry. Importantly, only 0.5% of +/del5 cells showed mCherry-positive signal (Fig. 2a), demonstrating a reduced capacity of these cells to repair DSBs by HR.

BRCA2-deficient cells accumulate ssDNA gaps in conditions of replication stress, such as PARPi or HU treatment[7,20,41]. We recently showed that PARPi- and HU-induced replication stress require distinct DNA-binding domains of BRCA2[8]. Given that the del5 variant conferred sensitivity to PARPi but not to HU, we tested whether +/del5 cells accumulated PARPi-induced ssDNA gaps using single-molecule DNA combing[42]. Following a first pulse with IdU, cells were pulsed with CldU in the presence of 30 μM PARPi for 2 h. After release, the cells were further incubated with or without S1 nuclease for 30 min; this enzyme creates nicks only in ssDNA regions, resulting in a shorter tract length[43]. We then measured the ratio of CldU/IdU in both conditions for each cell line. As expected, MCF10A did not show sensitivity to the S1 enzyme as manifested by an equal median CldU/IdU ratio of 1.5 before and after treatment with S1 (Fig. 2b). This was also the case for +/delT cells (median CldU/IdU ratio of 1.3 before and after S1 treatment). In stark contrast, +/del5 cells displayed high sensitivity to S1 nuclease as revealed by a consistent reduction in the CldU/IdU ratio (median CldU/IdU ratio 1.4 (-S1) to 1 (+S1)), suggesting that +/del5 cells accumulate PARPi-induced ssDNA gaps (Fig. 2b). These results agree with the observed sensitivity of +/del5 cells to PARPi (Fig. 1c). We further performed metaphase spreads after 24 h treatment with PARPi (10 μM) to detect the presence of ssDNA gaps or breaks in mitosis. Only +/del5 cells exhibited an increased frequency of aberrations, in particular chromatid breaks/gaps, under these conditions, whereas none of the cells showed this phenotype in untreated conditions (Fig. 2c).

Collectively, +/del5 cells exhibited a moderate decrease in HR capacity and accumulated PARPi-induced ssDNA gaps as revealed by S1-nuclease DNA combing and metaphase spreads. In contrast, +/delT cells showed normal DSB repair capacity and did not present detectable PARPi-induced ssDNA gaps.

Breast tumors with del5 and delT variants show comparable HRD mutational signatures and age at diagnosis, but exhibit variable LOH percentages

The phenotypes observed in our heterozygous cells suggested that a single mutation in BRCA2 might be sufficient to trigger genome instability and hence promote tumorigenesis. To shed light on this, we collected BRCA2 locus-specific LOH data from breast tumors bearing either one or the other variant, as LOH is the predominant way by which the second allele is inactivated[16]. We recovered data from previously published work[13,15,17,29,44], CRB of Institut Curie, Penn. University and N.N. Petrov National Medical Research Center of Oncology (index cases) gathering a total of 33 c.5946delT (delT) and 59 999del5 (del5) tumors (Supplementary Data 1). We found that the percentage of LOH in breast cancer patients was 67% for c.5946delT and 51% for 999del5 cases (Fig. 3a), suggesting that LOH is not a prerequisite for cancer. Moreover, the age at diagnosis was equivalent among the patients with tumors that have undergone LOH versus those that do not (Fig. 3b, del5 median age: 48.5 (LOH) vs 49 (no LOH); delT median age: 49 (LOH) vs 47 (no LOH)).

Breast tumors defective in *BRCA1/2* generally display a specific set of genetic patterns of mutations (mutational signatures) that is collectively referred to as the homologous recombination deficiency (HRD) signature. This pattern is thought to arise from the error-prone compensatory mechanisms that take place to repair DSB or collapsed forks when BRCA1/2 is not functional[45,46]. Given the differences we observed in the phenotype of breast epithelial cell lines bearing the delT and del5 mono-allelic pathogenic variants and the defective HR observed in the latter, we asked whether this phenotype correlated with a specific mutational pattern in tumors. To do so, we extracted DNA from a small cohort of breast cancer patients bearing the c.5946delT or 999del5 variant. When possible, we recovered frozen tumor samples and matched adjacent healthy tissue, or else we compared the pattern with DNA extracted from blood from the same patient. As we could only recover 3 tumors from carriers of the 999del5 variant, we also used previously published WGS data from 8 tumors bearing the same variant[45]. For the original samples, we performed WGS at 30X sequence depth, called the somatic mutations, and extracted the mutational signatures. In total, 7 delT tumors and 11 del5 tumors (8 previously reported[45] and 3 new) were analyzed. We found that all tumors exhibited one or more of the following signatures: base-substitution signature 3 (SBS3), SBS8, rearrangement signature 5, and copy number profile showing widespread LOH and deletion with microhomology (Fig. 3c, Supplementary Fig. 3) as generally found in *BRCA1/2* deficient tumors[46]. We used HRDetect[45], a WGS-based predictor of HR deficiency based on 5 different signatures. According to the genomic profiles, all tumors analyzed de novo (7 delT and 3 del5) scored above the 0.7 cutoff, indicating HRD signature (Fig. 3d) independently of their subtype or hormonal status (Supplementary Data 2).

https://doi.org/10.1038/s41467-025-67209-2

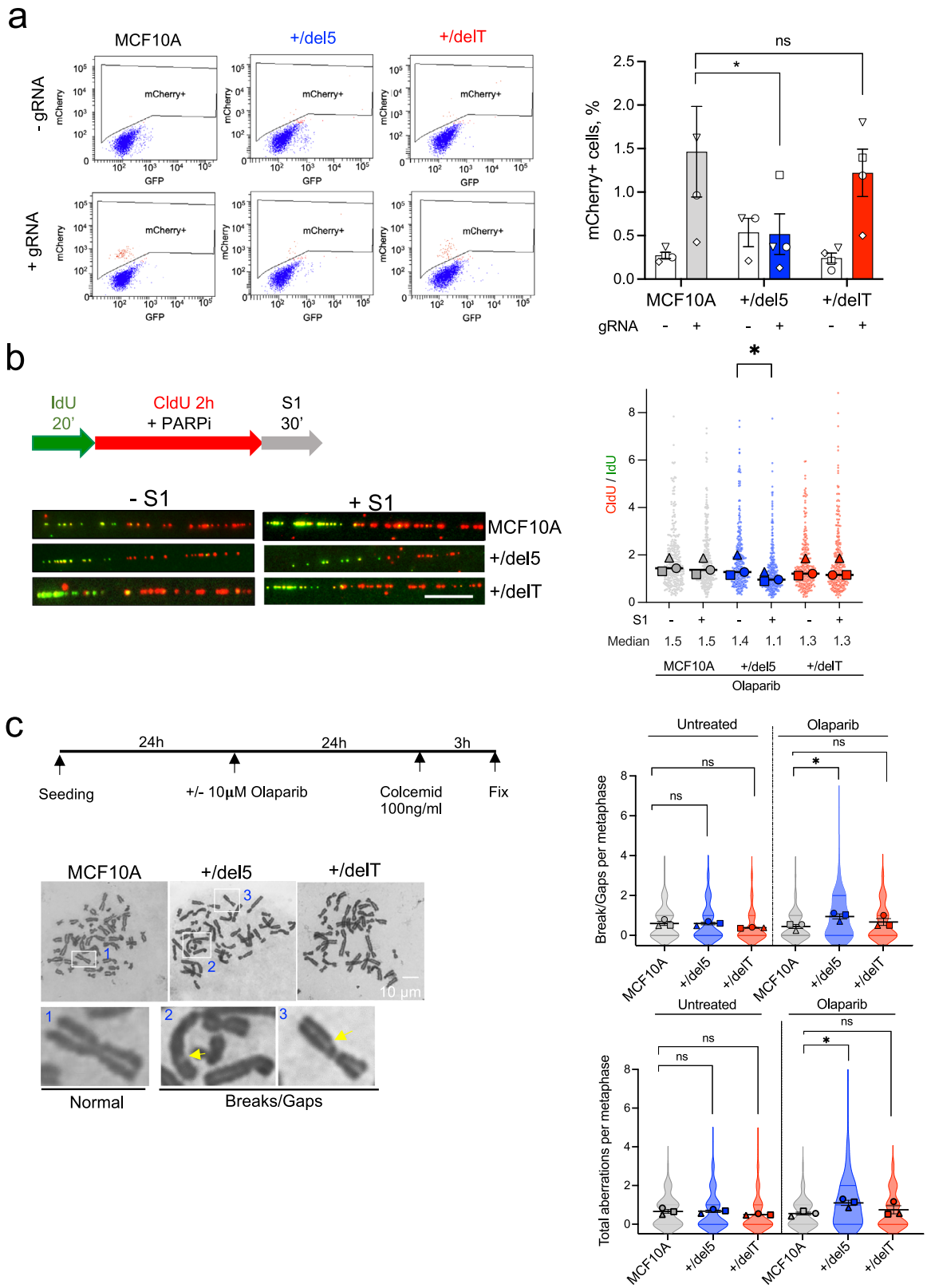

Together, 51-67% of tumors bearing c.5946delT and 999del5 truncating pathogenic variants showed LOH, suggesting a single mutation in *BRCA2* is sufficient for tumorigenesis. Moreover, BRCA2-locus LOH did not accelerate cancer onset in the 84 cases analyzed. Interestingly, despite the different genome instability features, both c.5946delT and 999del5 truncating pathogenic variants gave rise to a similar HRD mutational signature.

The BRCA2 delT pathogenic variant results in transcriptomic changes related to epithelial cell proliferation in cells and tumors

Given the apparent genomically stable phenotype of cells expressing the delT variant, we examined the transcriptome of these cells by RNA-seq. We took 3 sets of independent clones arising from the same screen (Fig. 1a, Supplementary Fig. 1a) to interrogate whether the two mono-

Fig. 2 | +/del5 cells show reduced HR capacity and accumulate PARPi-induced ssDNA gaps. a Representative flow cytometry gating and quantification of mCherry-positive cells as a readout of the HR assay[40] at 8 days post-transfection in MCF10A control and BRCA2-mutated cells. Cells were transfected with the promoter-less donor plasmid (AAVS1-2A-mCherry) without (empty bars) or with the gRNA, as indicated. Data represent mean ± SEM of four independent experiments (symbols indicate replicates). Statistical analysis by two-way ANOVA with Dunnett's multiple comparisons test. ns, not significant; *p = 0.0447 vs MCF10A. **b** Labeling scheme and representative DNA fiber images from MCF10A and BRCA2-mutated cells treated with 30 µM Olaparib followed by 30 min S1 nuclease (or buffer) treatment. Scale bar, 15 µm. Quantification of CldU/IdU ratio; each dot represents a fiber, with experiment means superimposed. n = 3; 100 fibers per condition. Statistical analysis by two-tailed paired ratio t-test (-S1 vs +S1). *p = 0.0376. **c** Experimental setup and representative metaphase images showing chromatid breaks/gaps in untreated or Olaparib-treated cells (10 µM, 24 h). Scale bar, 10 µm. Quantification of breaks/gaps (top right) and total chromosomal aberrations (bottom right) shown as violin plots with means overlaid. Statistical analysis by two-way ANOVA with Dunnett's multiple comparisons test. Breaks/gaps: ns, not significant; *p = 0.0117. Total aberrations: ns, not significant; *p = 0.0108. 40 metaphases among three independent experiments per condition were scored. All the experiments in the Figure were performed with clone #1 of +/delT and +/del5 cells. Source data are provided as a Source Data file.

allelic variants resulted in any gene expression changes. As controls, we used the parental cell line (MCF10A, Ctrl #2) and two clones from either the del5 screen (Ctrl #1) or the delT screen (Ctrl #3) that did not result in gene-edited BRCA2. After selecting protein-coding genes and filtering out the genes with low expression, we pursued the analysis with 13,842 genes. Principal component analysis (PCA) discriminated +/delT clones from the MCF10A and +/del5 clones, explaining 36% of the variance by PC1 (Supplementary Fig. 4a). The comparison among the 3 biological replicates of +/delT resulted in ~5% of the protein-coding transcriptome rewired: 781 differentially expressed genes (DEGs) (268 up and 513 down) (log2 fold change > 1.5 and adj. p-value 0.05) compared to the wild type counterparts (Fig. 4a, Supplementary Data 3). In contrast, +/del5 cells showed no DEGs (Fig. 4b). Gene Ontology (GO) enrichment analysis of biological processes indicated that +/delT cells exhibited deregulated pathways related to epithelial cell migration and proliferation (Fig. 4c).

Next, to find out whether the DEGs observed in +/delT MCF10A cells were relevant in tumors, we collected RNA from 9 primary tumors and matched non-neoplastic adjacent tissue of breast cancer patients carrying the same germline mutation (c.5946delT), 7 of which were used for the mutational signature analysis (Fig. 3c, d), and performed RNA-seq. We selected protein-coding genes and discarded those with low expression (n = 14,479). A log2 fold change (LFC) of 1.5 (adj. p-value < 0.05) was set to consider DEG compared to the matched adjacent tissue. In delT tumors, 1079 genes appeared upregulated and 1521 downregulated (Supplementary Data 4). The top three deregulated genes were primarily associated with embryonic organ development, actin filament organization, and epithelial cell proliferation (Fig. 4d). Although we did not have access to RNA from del5 tumor samples, we analyzed four previously published RNA-seq datasets from del5 tumors and five healthy controls, two of which carried BRCA2 mutations (ref. 46). Some of these tumor samples had previously been used for whole-genome sequencing (WGS) analysis in Fig. 3. Although the healthy controls used in the analysis were not patient-matched, they were processed using the same protocols and analytical pipeline. Importantly, they clustered together in the principal component analysis (PCA) plot, supporting their consistency and suitability for comparative analysis (Supplementary Fig. 4b). Differential gene expression analysis revealed that the del5 tumors exhibited markedly fewer transcriptional changes compared to delT tumors, as shown in the volcano plots (Supplementary Fig. 4c). A strong correlation (R = 0.92) was observed between the number of DEGs and deregulated GO BP terms across samples, the delT tumors showing the highest deregulation (Supplementary Fig. 4d). Gene Ontology Biological Process (GO BP) analysis identified only five deregulated GO BP terms in del5 tumors (Fig. 4e) versus 1,189 in delT tumors (out of 4,953 total GO BP terms), with a Fisher's exact test p-value of 2.2×10^{-16} (Supplementary Fig. 4e). Notably, these findings were consistent with our observations in MCF10A +/del5 versus +/delT cells as illustrated in the number of DEGs in cell lines and tumors (Fig. 4f).

In summary, expression of the delT variant led to extensive global transcriptomic alterations in both MCF10A cells and tumors, whereas the del5 variant induced minimal changes in both cells and tumors. Notably, the deregulated pathways in +/delT cells were enriched for epithelial cell proliferation processes, consistent with findings from the delT tumor cohort.

+/delT cells display a slower proliferation rate and reduced migration capacity in 2D, while increasing the invasion capacity in 3D

Given that the delT mutation altered genes involved in cell migration and proliferation, we interrogated the capacity of +/delT cells to grow and form colonies. We monitored the proliferation of these cells over seven days. Interestingly, the proliferation rate of +/delT cells measured by an Incucyte system was reduced (Fig. 5a, Supplementary Fig. 5a) compared to the +/del5 and MCF10A parental cells, despite a cell cycle profile unchanged (Supplementary Fig. 5b). Moreover, +/delT cells adopted a 'fibroblast-like' shape in contrast to the cuboidal shape of MCF10A and +/del5, typical of epithelial cells. This manifested in a different pattern of actin staining and reduced circularity in +/delT cells compared to the other cell lines (Fig. 5b).

Given the changes in cell shape and the gene expression changes related to epithelial cell proliferation and migration observed in the +/delT cells and tumors, we monitored the vimentin levels, a cytoskeletal protein that regulates cell migration and shape and has been associated with epithelial-to-mesenchymal transition (EMT)[47]. Remarkably, +/delT displayed reduced vimentin cellular intensity as compared to MCF10A and the +/del5 cells (Fig. 5c). Correcting the mutation (+/revdelT) (Supplementary Fig. 1e) restored the levels of vimentin (Fig. 5c), suggesting the changes observed were specifically due to the delT variant.

To confirm the changes in epithelial cell migration directly, we performed a scratch wound-healing assay[48]. First, a confluent monolayer of cells was serum-starved for 24 h and released into a medium with 2% serum to limit cell growth. Under these conditions, a linear scratch was created using a 10 µl pipette tip, after which the closure of the wound was monitored at times 0 h and 16 h after incubation at 37 °C. +/delT cells showed reduced wound closure capacity compared to the parental MCF10A cells or the +/del5 cells (Fig. 5d, Supplementary Fig. 5c). This phenotype was partially restored in the +/revdelT-cells and was not due to differences in cell proliferation as the levels of the cell proliferation marker Ki67 were comparable under these growth conditions (i.e., 2% serum) (Fig. 5d). We then monitored the capacity of the cells to individually form colonies as these features could be relevant for transformation. Despite its slower proliferation rate and reduced migration, +/delT cells showed normal colony formation potential or even slightly higher than the controls (Supplementary Fig. 5d). This prompted us to test their anchorage-independent growth capacity in soft agar, a well-established method to evaluate the transformation potential of cells[49]. We used breast epithelial cancer cells MCF7 as a reference, as they are known to grow under these conditions. MCF7 cells showed a median colony size of 2080 µm^2, whereas MCF10A cells showed much smaller colonies, as expected (median of 537 µm^2). Similar to MCF10A cells, +/del5 cells showed a median colony size of 474 µm^2. Remarkably, +/delT showed a 2-fold increased colony size (1143 µm^2) compared to MCF10A or +/del5

https://doi.org/10.1038/s41467-025-67209-2

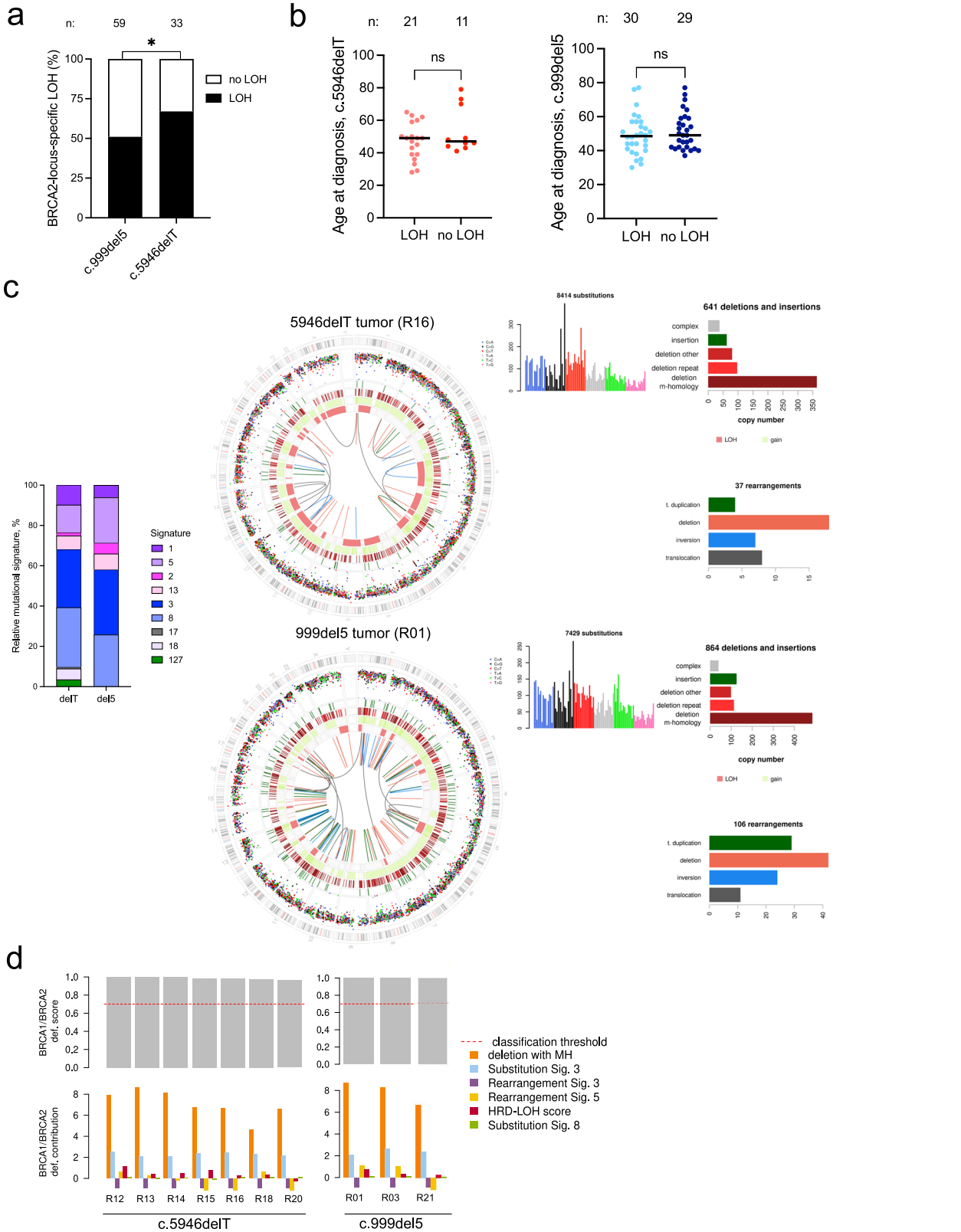

Fig. 3 | Breast tumors with 999del5 and c.5946delT variants show comparable HRD mutational signatures and age at diagnosis, but exhibit variable LOH percentages. a Frequency of LOH at the BRCA2 locus in tumors carrying c.5946delT (n = 33) or 999del5 (n = 59) variants. Statistical analysis by two-tailed Fisher's exact test; *p = 0.0308. **b** Age at diagnosis for patients with c.5946delT (left, n = 32) or 999del5 (right, n = 59) variants, stratified by LOH status. Statistical analysis by two-tailed unpaired t-test; ns, not significant. **c** Mutational signature composition in 7 BRCA2 delT and 11 BRCA2 del5 primary tumors (left). Representative circos plots of genome profiles for one delT and one del5 tumor (right), showing: (I) karyotypic ideogram; (II) base substitutions (blue, C > A; black, C > G; red, C > T; gray, T > A; green, T > C; pink, T > G); (III) insertions (green lines); (IV) deletions (red lines); (V) copy number changes (green, gain; red, loss); (VI) rearrangements (green, duplication; red, deletion; blue, inversion; gray, translocation). Adjacent histograms show counts for substitution signatures (top), indels (middle), and rearrangement signatures (bottom). **d** HRDetect scores per sample (top); threshold at 0.7 (red dotted line). Contribution of each mutational signature to the HRD score per sample (bottom). Source data are provided as a Source Data file.

(Fig. 5e). Importantly, +/revdelT cells restored the size of the colonies to MCF10A levels (Fig. 5e), confirming the effect was due to the delT variant.

To mimic cell growth in the mammary gland, we plated MCF10A clones on Basement Membrane Extract (BME) gel to generate organoids[50]. In these settings, all three cell lines formed multicellular organoids embedded in the medium (Fig. 5f). Interestingly, +/delT organoids grew bigger colonies compared to the parental MCF10A counterparts, and this phenotype was restored in the +/rev delT organoids (Fig. 5f), recapitulating the results obtained in soft-agar (Fig. 5e). In contrast, +/del5 organoids grew smaller colonies than the MCF10A cells (Fig. 5f). Consistently, spheroid-like structures from +/delT cells showed higher invasion capacity in collagen gel than MCF10A parental cells (Fig. 5g).

Together, these results indicate that +/delT cells show decreased vimentin levels, reduced cell proliferation and circularity, and decreased cell migration capacity in 2D, while increasing colony formation capacity of MCF10A in two anchorage-independent conditions in 3D and higher invasion potential in a spheroid setting. In contrast, +/del5 cells displayed similar levels of vimentin and similar shape and migration capacity to MCF10A cells while reducing the organoid size.

The delT variant induces epigenetic changes in the NF-κB signaling pathway by sequestering the acetyltransferase PCAF

BRCA2 comprises a transactivation domain in its N-terminus[51] whose activity requires its interaction with the acetyl-transferase PCAF[12]. Given the large transcriptomic changes observed in +/delT cells, we hypothesized that the truncated product of BRCA2 resulting from the expression of the delT variant, which comprises both the predicted transactivation domain and the PCAF-interacting region, could be interfering with the transactivation activity of the wt allele of BRCA2 in the nucleus in a dominant negative fashion. To test this idea, we first set out to detect the truncated BRCA2 protein in +/delT cells with a predicted molecular weight of 224 kDa. Using an antibody raised against the N-terminal region of BRCA2 (validation in Supplementary Fig. 5b), we detected a weak band around the 250 kDa marker at the position at which this product runs in CAPAN-1 cells (Fig. 6a), a pancreatic cancer cell line expressing 3 copies of the same delT polypeptide[52]. We also performed nuclear/cytoplasmic fractionation (Supplementary Fig. 6a) and found the same band in the nucleus of +/delT cells but not in +/del5 or MCF10A cells, supporting the presence of the delT product in the nucleus of +/delT cells. We did not observe any band corresponding to the size expected for the del5 product (~40 kDa) (Supplementary Fig. 6b), in agreement with a previous report[36]. Consistently, the delT product was located almost exclusively in the nucleus in CAPAN-1 cells, similarly to PCAF, as manifested by nuclear/cytoplasmic fractionation performed in these cells (Fig. 6b).

Previous work reported that the transient depletion of BRCA2 in breast epithelial cells supports survival in epidermal growth factor (EGF)-depleted conditions of the same cells once the expression of BRCA2 is recovered. This phenomenon was linked to the activation of the NF-κB pathway and an increased histone H4 acetylation[19]. Given that EGF induces NF-κB activation[53] and that this pathway is related to migration and proliferation altered in +/delT cells and delT tumors, we tested the proliferation in EGF-depleted conditions and the levels of H4 acetylation and NF-κB activation. Using an MTT assay, we measured the fraction of surviving cells in the presence or absence of EGF. Consistent with the proliferation results (Fig. 5a), in normal growth media (+EGF), the survival was reduced in +/delT compared to the MCF10A cells; in contrast, the absence of EGF did not affect further their survival whereas it reduced that of the MCF10A cells (Supplementary Fig. 6c). We therefore performed western blot analysis to detect the levels of acetylation of histone H4 and the activation status of NF-κB monitoring the phosphorylation of the p65 (RELA) subunit at S536. Strikingly, +/delT cells showed reduced levels of both H4 acetylation (K5, K8, K12, K16) and NF-κB activation (p65-pS536), whereas +/del5 showed similar levels compared to the MCF10A cells (Fig. 6c). Importantly, these changes were partially restored in the +/revdelT cells (Fig. 6d), indicating they are linked to the delT variant.

Given the known transcriptional activity of NF-κB, we examined the mRNA levels of NF-κB target genes from our RNA-seq data in +/delT cells compared to the MCF10A and +/del5 cells. Consistent with reduced p65-pS536 levels, Gene set enrichment analysis (GSEA) of three curated RELA target gene subsets (*RELA*_targets_inflammatory, *RELA*_targets immune costim, RELA targets matrix_invasion[54] revealed significant negative enrichment of the inflammatory subset in +/delT cells compared to +/del5 and control MCF10A cells (NES = −1.824; adj. p = 0.00088), indicating transcriptional downregulation of *RELA*-driven inflammatory programs. Heatmap analysis confirmed reduced expression of canonical NF-κB targets (*IL6*, *CXCL1, CXCL3*, *TNFAIP3*, *NFKBIA*) in +/delT clones and not in +/del5 cells, supporting suppression of NF-κB-mediated inflammatory signaling in +/delT clones (Fig. 6e). This particular subset was not significantly altered in delT tumors; however, Gene Set Enrichment Analysis (GSEA) and heatmap visualization of RELA target genes revealed a general downregulation in RELA-driven inflammatory genes suggesting suppression of NF-κB-mediated inflammation (Supplementary Fig. 6d, e) as observed in +/delT cells. In contrast, del5 tumors exhibited a more heterogeneous expression pattern, with several genes maintaining expression levels comparable to the healthy controls (Supplementary Fig. 6f).

To further investigate the mechanism behind these alterations, we monitored NF-κB nuclear translocation to the nucleus. The levels of nuclear p65 were comparable between MCF10A and +/delT cells (Supplementary Fig. 7a), suggesting that NF-κB translocation is not impaired in +/delT cells. We next examined whether the delT BRCA2 product could sequester PCAF by performing immunoprecipitation (IP) of BRCA2 from nuclear extracts of MCF10A and +/delT cells using an N-terminal BRCA2 antibody. Consistent with a previous report[12], PCAF co-immunoprecipitated with BRCA2 in both cell types, with a modest increase in PCAF signal observed in +/delT cells (Supplementary Fig. 7b). To determine whether the truncated BRCA2 delT product could independently associate with PCAF, we performed BRCA2 immunoprecipitation (IP) in CAPAN-1 cells, which lack full-length BRCA2. PCAF robustly co-immunoprecipitated with the delT product, indicating that the truncated variant is sufficient to form a complex with PCAF (Fig. 6f). Given the low abundance of the delT product in +/delT cells, we hypothesized that it may sequester PCAF by forming aberrant oligomers with full-length BRCA2. To test this, we co-expressed GFP-MBP−tagged delT and MBP-BRCA2-RFP in HEK293T cells and performed a GFP-trap assay. As previously shown[53], GFP-MBP−BRCA2 formed a complex with MBP-BRCA2-RFP, unlike the GFP-MBP tag-only control. Importantly, GFP-MBP−delT also associated with MBP-BRCA2-RFP, and this complex co-immunoprecipitated with PCAF, supporting the hypothesis that the delT product can sequester PCAF through oligomerization with full-length BRCA2 (Fig. 6g). Moreover, overexpression of GFP-delT in HEK293T cells led to a dose-dependent increase in PCAF co-immunoprecipitated with endogenous full-length BRCA2, consistent with a sequestration mechanism (Supplementary Fig. 7c).

A positive feedback loop has been described in which p65 phosphorylation promotes its interaction with the acetyltransferase P300/CBP, leading to H4 acetylation and sustained NF-κB activation[55]. Although this mechanism has not been reported for PCAF, PCAF acetylates both NF-κB and histones H3/H4[56] and interacts with P300/CBP[57], suggesting a similar regulatory axis may exist. To test this, we examined whether BRCA2 could form complexes with PCAF and P300. BRCA2 co-immunoprecipitated with both PCAF and P300 when overexpressed in HEK293T cells (Supplementary Fig. 7d). Although P300 levels were low in MCF10A cells, inhibition of NF-κB using IMD 0354 reduced both p65

https://doi.org/10.1038/s41467-025-67209-2

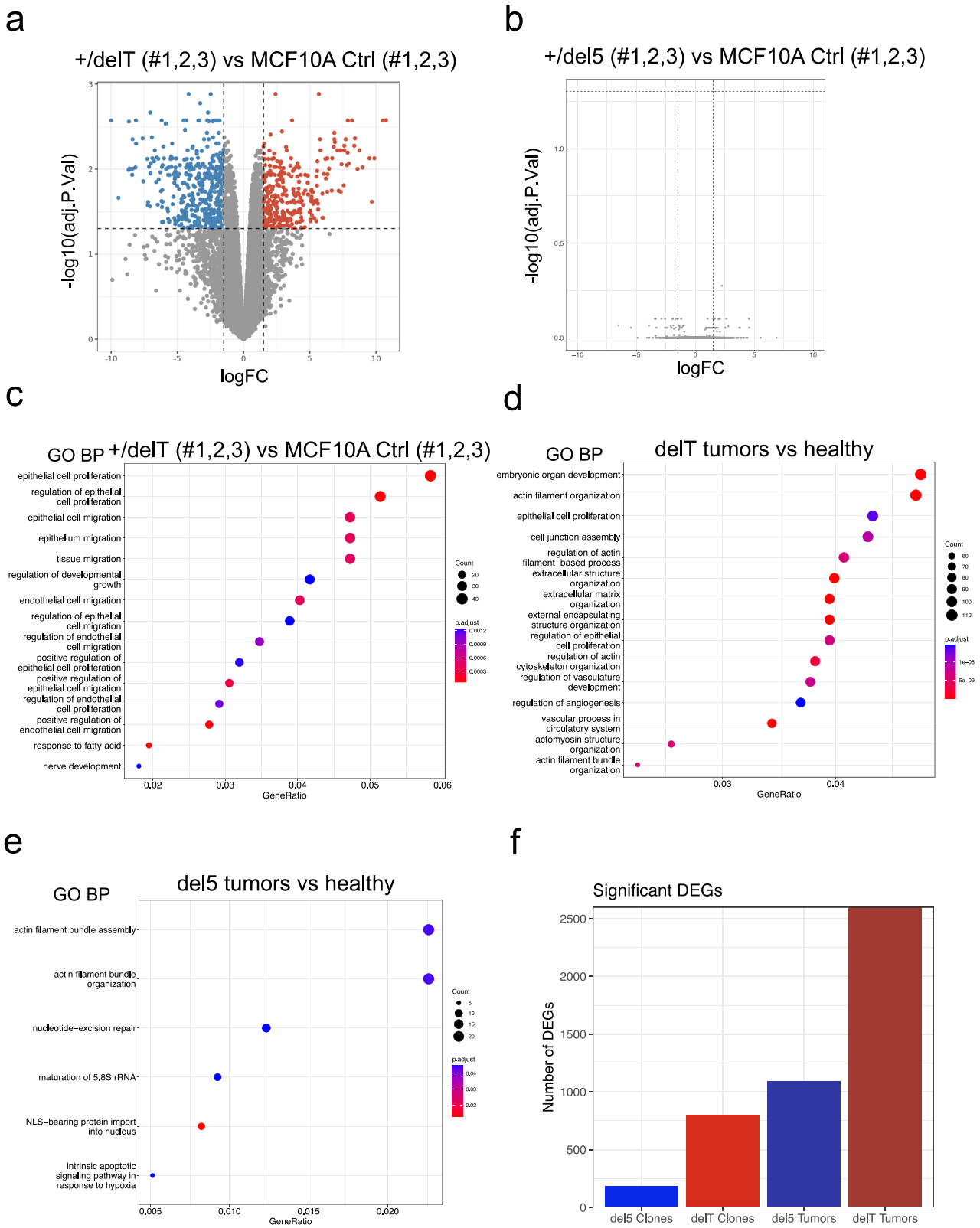

Fig. 4 | BRCA2 delT pathogenic variant induces transcriptomic changes linked to epithelial cell proliferation in cells and tumors. a Volcano plot showing differentially expressed genes (DEGs) in +/delT clones (n = 3) vs MCF10A controls (n = 3). Upregulated genes (red) and downregulated genes (blue) were defined by $\log_2$ fold change >1.5 and adjusted $p < 0.05$. **b** Same analysis as in (**a**) for +/del5 clones. **c** Bubble plot of GO Biological Processes enriched among DEGs in +/delT clones vs MCF10A controls, ranked by adjusted p-value (color scale: red to blue). **d** Bubble plot of top GO BP terms enriched in DEGs from 9 delT tumors vs matched adjacent normal tissues (Supplementary Data 2), using the same DEG filtering parameters and GO analysis pipeline. **e** Same analysis as in (**d**) for 4 tumors with the 999del5 variant and 5 healthy controls (ref. 46) (Supplementary Table 2). For **c**–**e**, we used a one-sided hypergeometric test with a correction for multiple comparisons using Benjamini-Hochberg and an adjusted p-value threshold of 5%. **f** Number of significant DEGs in del5 and delT clones and tumors.

https://doi.org/10.1038/s41467-025-67209-2

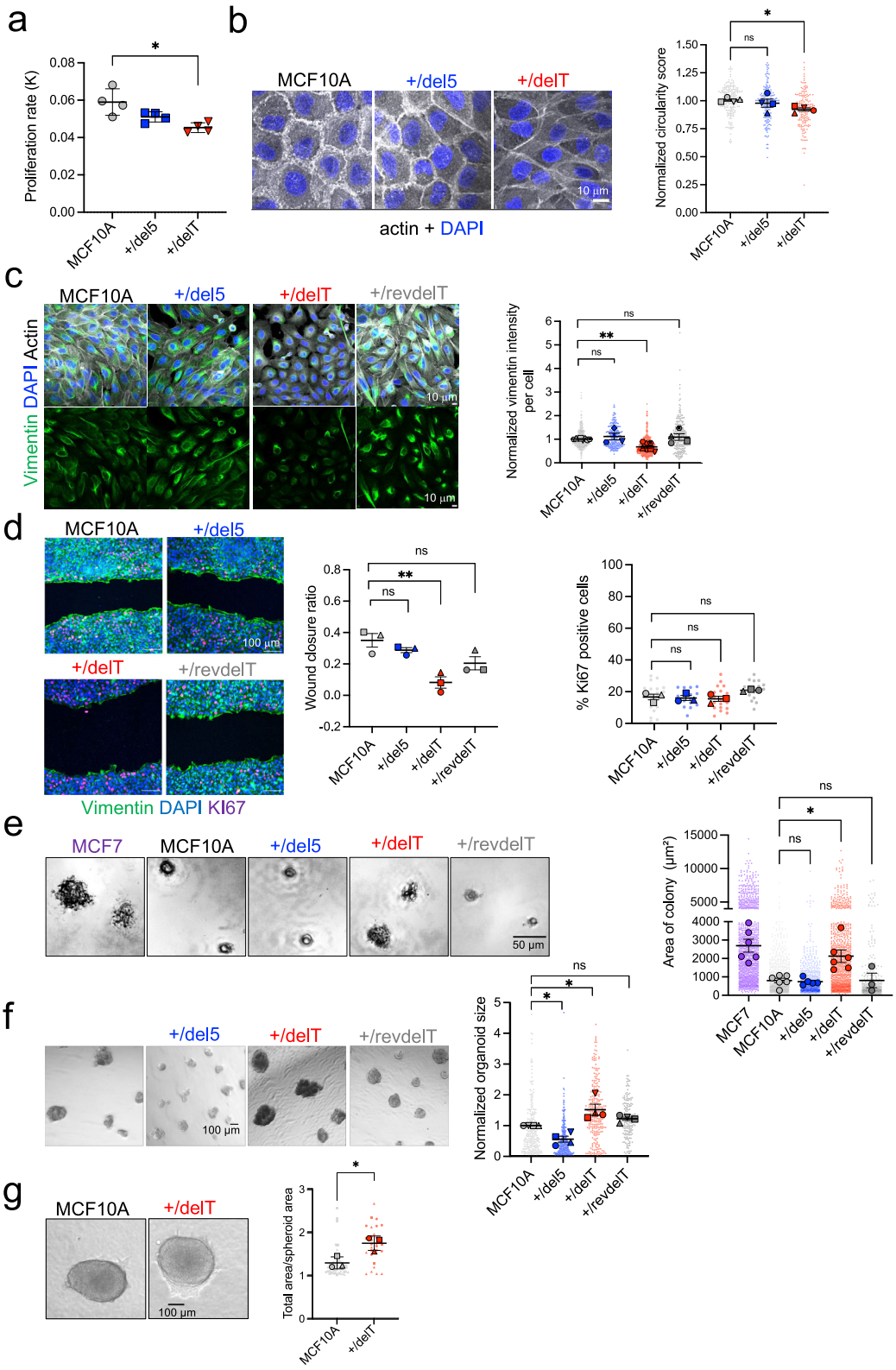

pS536 and H4 acetylation, supporting the existence of a feedback loop involving these factors (Supplementary Fig. 7e).

In summary, the BRCA2 delT product localized to the nucleus in both +/delT and CAPAN-1 cells. Unlike +/del5 cells, +/delT cells showed reduced H4 acetylation and p65 pS536 levels, which were partially restored upon correction of the delT mutation. EGF promoted proliferation in control MCF10A cells but not in +/delT cells, likely due to impaired NF-κB activation. Transcriptomic analysis revealed broad downregulation of NF-κB target genes in +/delT cells and tumors, but not in +/del5 counterparts. The delT product associated with PCAF in CAPAN-1 cells and formed aberrant oligomers with full-length BRCA2 and PCAF in HEK293T cells. BRCA2 formed complexes with PCAF and P300/CBP when overexpressed in HEK293T cells and inhibiting NF-κB reduced the levels of H4 acetylation.

Fig. 5 | +/delT cells show reduced proliferation and migration in 2D, while increased invasion in 3D. a Proliferation of the indicated cell lines over 7 days (n = 4). Statistical analysis by Kruskal–Wallis with Dunn's multiple comparisons test; *p = 0.0134. **b** (**Left**) Representative F-actin (white) and DAPI (blue) staining of MCF10A cells. Scale bar, 10 µm. (**Right**) Quantification of cell circularity from actin staining (n = 4; 46 cells/experiment), normalized to MCF10A. Kruskal–Wallis with Dunn's test; *p = 0.0285; ns, not significant. **c** (Left) Representative vimentin (green), actin (white), and DAPI (blue) staining. Scale bar, 10 µm. (Right) Quantification of vimentin intensity per cell (n = 4; 50–80 cells/condition). Kruskal–Wallis with Dunn's test; **p = 0.0030; ns, not significant. **d** (Left) Scratch wound assay images stained for vimentin (green), Ki67 (magenta), and DAPI (blue) at 16 h. (Middle) Quantification of wound closure (n = 3; 6–10 wounds/condition). One-way ANOVA with Dunnett's test; **p = 0.02; ns, not significant. (Right) Percentage of Ki67-positive cells; ns, not significant. **e** (Left) Soft agar assay images of MCF10A clones and MCF7 cells stained with crystal violet after 14 days. (Right) Quantification of colony area (n = 6; +/revdelT, n = 3). Kruskal–Wallis with Dunn's test; *p = 0.0385 vs MCF10A. **f** (Left) Brightfield images of organoids from MCF10A, +/del5, +/delT, and +/revdelT cells at day 12. (Right) Quantification of organoid area (n = 4). One-way ANOVA with Dunnett's test; *p = 0.0317 (MCF10A vs +/del5), *p = 0.0119 (MCF10A vs +/delT); ns, not significant. **g** (Left) Brightfield images of spheroids embedded in collagen gels after 24 h. (Right) Quantification of invasion area (n = 3). Paired t-test; *p = 0.0492. All experiments used clone #1 for MCF10A, +/delT, and +/del5. All the data in this figure are represented as mean ± SEM. Source data are provided as a Source Data file.

These findings support a model in which the BRCA2 delT variant disrupts NF-κB signaling by aberrantly engaging PCAF and P300, leading to reduced histone acetylation and impaired transcriptional activation.

Overexpression of PCAF partly rescues the NF-κB target gene expression and the phenotype of +/delT cells

To further support the link between PCAF acetyltransferase and the transcriptomic changes observed in the +/delT cells, in particular of NF-κB-related genes, we overexpressed either PCAF-GFP or GFP as a control in +/delT cells and performed qRT-PCR for six known NF-κB target genes that were downregulated in the +/delT cells by RNA-seq (Fig. 7a). We noticed that the transfection itself induced NF-κB activity, so we analyzed the mRNA levels six days post-transfection.

We first analyzed the expression of these genes in +/delT vs MCF10A and confirmed by qRT-PCR the downregulation of *CXCL1*, *IL6*, *VIM*, *CXCL3*, *CXCL8*, and *NFKBIZ* We also confirmed that the mRNA levels of *RELA* and *PCAF* remained unchanged. (Supplementary Fig. 8a). Interestingly, transfecting +/delT cells with PCAF-GFP was sufficient to increase the mRNA levels of *CXCL1* and *VIM* without altering the mRNA levels of *RELA* compared to the same cells transfected with the empty vector (GFP) (Fig. 7a). A general increasing trend was also observed for *IL6*, *CXCL3*, *CXCL8* and *NFKBIZ* although it was not statistically significant probably due to the variability of transfection efficiency revealed by the different *PCAF* expression levels among the experiments (Supplementary Fig. 8b). Consistent with the overall recovery of the expression of these genes, overexpression of PCAF-GFP restored two of the phenotypes observed in the +/delT cells: it increased the vimentin protein intensity levels as detected by immunofluorescence (Fig. 7b) and it reduced the organoid growth of +/delT cells (Fig. 7c) compared to the GFP-alone transfected cells.

Together, overexpression of PCAF partially rescued the mRNA levels of NF-κB-related genes tested, especially *CXCL1* and *VIM*. Accordingly, this was also sufficient to revert two of the phenotypes observed in +/delT cells: the reduced vimentin intensity levels and the increased organoid growth.

Discussion

In this work, we interrogated whether BRCA2 heterozygosity confers haploinsufficiency by recreating two of the most common truncating pathogenic variants in non-malignant breast epithelial cells. Surprisingly, we found that these two variants led to markedly different outcomes in heterozygosis.

+/del5 cells exhibited reduced levels of BRCA2 and RAD51, along with genomic instability features such as increased sensitivity to mitomycin C (MMC) and PARP inhibitors (PARPi), reduced homologous recombination (HR) capacity, and the accumulation of PARPi-induced single-stranded DNA (ssDNA) gaps. Consistent with these cellular phenotypes, tumors harboring the 999del5 variant displayed an HR-deficiency (HRD) mutational signature. These results support the notion that BRCA2 truncating variants that are not expressed can confer haploinsufficiency.

Moreover, two additional clones isolated from the +/del5 screen (+/del5 #2 and +/del5 #3, see Methods), which harbored truncating mutations resulting in nearby but distinct stop codons, recapitulated the key phenotypes observed in the original +/del5 cells. Specifically, these clones exhibited sensitivity to PARPi, reduced BRCA2 protein levels, and an unaltered transcriptome relative to parental MCF10A cells. These findings strongly support the idea that truncating BRCA2 mutations that are not expressed as stable protein products yield similar functional consequences, as exemplified by the 999del5 variant.

In stark contrast, +/delT cells maintained normal levels of full-length BRCA2 and RAD51, exhibited hyper-resistance to PARPi and MMC, preserved HR capacity, and did not accumulate PARPi-induced ssDNA gaps. Interestingly, +/delT cells exhibited widespread transcriptional dysregulation, affecting approximately 5% of protein-coding genes, with a pronounced impact on pathways related to epithelial cell migration and proliferation—features not observed in +/del5 cells. Consistently, breast tumors harboring the 5946delT variant demonstrated extensive transcriptional rewiring, including alterations in epithelial migration and proliferation pathways, alongside a general downregulation of key NF-κB target genes, closely mirroring the transcriptomic profile of +/delT cells. In contrast, these changes were absent in tumors expressing the 999del5 variant, reinforcing the alignment between our cellular models and tumor-derived data. This transcriptional reprogramming in +/delT cells was accompanied by reduced global histone H4 acetylation and diminished activation of the NF-κB p65 subunit.

Functionally, +/delT cells exhibited reduced proliferation, decreased vimentin expression, and impaired collective migration in 2D cultures. However, they demonstrated enhanced growth in anchorage-independent conditions, increased organoid formation, and greater invasiveness in 3D collagen matrices—features indicative of a shift toward an invasive phenotype.

The delT polypeptide lacks the nuclear localization signals located at the C-terminus of BRCA2 and was shown to be mainly located in the cytoplasm in human pancreatic cancer cells, CAPAN-1, when overexpressed with a GFP tag[34]. Using the same cell line, we detected the endogenous delT product almost exclusively in the nucleus. This discrepancy might arise from the overexpression of the GFP-delT product in the previous work.

How is the delT polypeptide located in the nucleus? PALB2 is a protein described to localize BRCA2 to the nucleus[58]; the region of interaction with PALB2 is encompassed in the delT product, which could promote delT nuclear localization.

How does the delT product, which is expressed in low amounts, produce such a transcriptional and acetylation rewiring in the +/delT cells? BRCA2 has been reported to form self-interacting complexes that preferentially engage the N-terminal and C-terminal regions of the protein[59–61]. We show here that the delT product associates with the full-length BRCA2 protein in the form of aberrant oligomers that contain PCAF, supporting the idea that the delT product "sequesters" PCAF.

https://doi.org/10.1038/s41467-025-67209-2

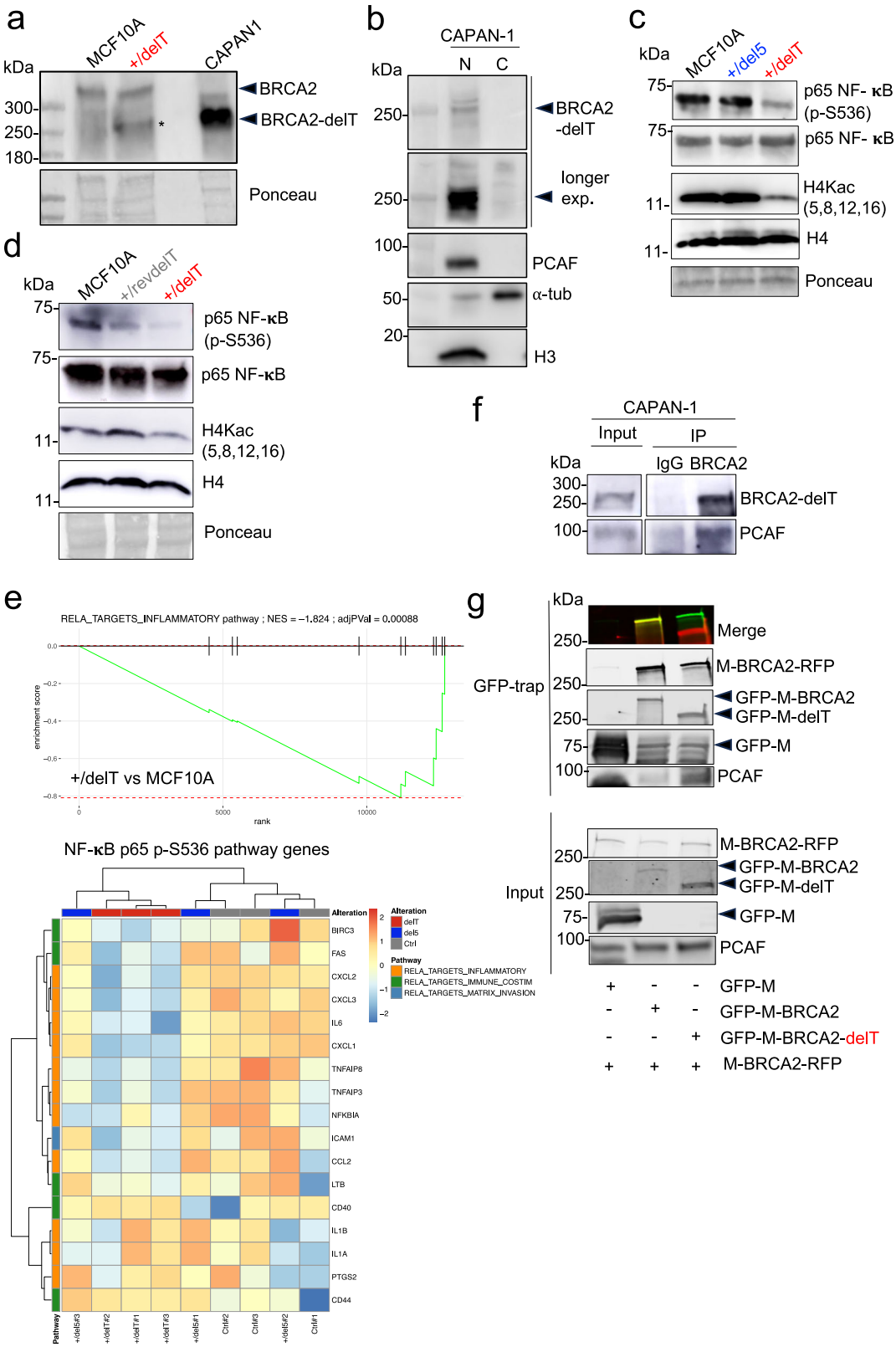

What is the link between PCAF, acetylation of H4, and NF-κB activation? A positive feedback loop has been described for H4 acetylation and p65 phosphorylation: p65 phosphorylation promotes the binding of p65 to the acetyltransferase P300/CBP and the acetylation of H4. H4 acetylation enhances NF-κB gene transcription, further sustaining NF-κB activation[55]. We show here that P300/CBP is also in complex with BRCA2 and PCAF when overexpressing BRCA2 in HEK293T cells and that both phosphorylation of p65 and H4 acetylation are reduced when inhibiting NF-κB activation. Thus, we propose that BRCA2-bound PCAF gets recruited to phosphorylated p65, promoting H4 acetylation and NF-κB binding to its target genes to activate transcription. In the +/delT cells, delT-sequestered PCAF (and presumably P300) limit H4 acetylation precluding full access of NF-κB to its target genes, explaining the general downregulation of a subset of

Fig. 6 | The delT variant induces epigenetic changes in NF-κB signaling via PCAF sequestration. a Western blot showing the truncated BRCA2-delT product in the indicated cell lines, detected using an antibody against the N-terminal region of BRCA2 (Genscript). CAPAN-1 cells expressing only the delT product serve as a control. Asterisk indicates the predicted size of the truncated protein (n = 2). **b** Immunoblot of BRCA2-delT and PCAF in cytoplasmic (C) and nuclear (N) fractions of CAPAN-1 cells. α-tubulin and histone H3 serve as fractionation controls. Representative image of two independent experiments. **c** Western blot of acetylated histone H4 (K5, K8, K12, K16) and phosphorylated NF-κB p65 (S536) in MCF10A, +/del5, and +/delT cells (n = 3). **d** Western blot of acetylated histone H4 (K5, K8, K12, K16) and phosphorylated NF-κB p65 (S536) in MCF10A, +/delT, and +/revdelT cells (n = 2). **e** (**Top**) Heatmap of curated NF-κB-regulated inflammatory genes across +/delT, +/del5, and control clones, with pathway-level enrichment scores for RELA_TARGETS_INFLAMMATORY, IMMUNE_COSTIMULATION, and MATRIX_INVASION. Samples and corresponding genes are clustered using correlation as a dissimilarity metric, applying a two-sided test. (**Bottom**) GSEA plot showing significant negative enrichment of RELA_TARGETS_INFLAMMATORY in +/delT clones (NES = −1.824; adjusted p = 0.00088). **f** Co-immunoprecipitation of BRCA2 and PCAF in CAPAN-1 cells expressing the delT product. Rabbit IgG used as control (n = 2). **g** GFP-trap pull-down of GFP-MBP-BRCA2 WT, GFP-MBP-NLS (negative control), or GFP-MBP-delT co-transfected with MBP-BRCA2-WT-RFP in HEK293T cells. Complexes were analyzed by SDS-PAGE and immunoblotting with anti-GFP and anti-RFP antibodies (n = 2). Experiments in (**a**, **c**, **d**) were performed using clone #1 for MCF10A, +/delT, and +/del5. Source data are provided as a Source Data file.

NF-κB target genes observed in +/delT cells (Fig. 6e) and overall downregulation of the pathway observed in delT tumors (Supplementary Fig. 6e). This model is further supported by the following results: 1. H4 acetylation and NF-κB phosphorylation are partially restored in the CRISPR-corrected +/revdelT cells. 2. Overexpression of PCAF in +/delT cells rescues a subset of NF-κB target gene expression. 3. Overexpression of PCAF in +/delT cells rescues the vimentin levels and reduces organoid growth. 4. The overall downregulation of NF-κB observed in delT cells and tumors is not detected in +/del5 cells nor in tumors harboring this variant.

Our results strongly suggest that the BRCA2-PCAF complex modulates epithelial cell migration genes through the NF-κB signaling pathway and reveal this activity as a possible contributor to its tumor suppressor function. Interestingly, this pathway and H4 acetylation were shown to be upregulated in conditions of transient depletion of BRCA2, conferring proliferating advantage in EGF-deprived medium[19] in a model of non-transformed human breast epithelial cells. In contrast, another report showed the NF-κB signaling pathway was downregulated in prophylactic mastectomy-derived $BRCA2^{mut/+}$ progenitor cells and non-transformed mammary epithelial cells knocked down for BRCA2[18]. These discrepancies might arise from the use of different model systems or, rather, reflect the possible dissimilarities between distinct variants as we observe in this study. Nevertheless, these reports and our work reinforce the idea that the NF-κB signaling pathway plays a role in *BRCA2*-linked tumorigenesis, and we attribute this function, at least in part, to the association of BRCA2 with PCAF.

+/delT cells showed hyper-resistance to MMC and PARPi compared to MCF10A cells. These findings were surprising given the unchanged levels of BRCA2 and RAD51 protein in these cells. One possibility is that the global decreased H4 acetylation observed in +/delT cells protects the DNA of these cells from damage, consistent with the reduced number of γH2AX foci observed by QIBC upon MMC treatment in these cells. Moreover, PCAF acetyltransferase activity on histone H4 has been shown to promote the recruitment of MRE11 and EXO1 nucleases to resect DNA at replication forks, an activity that is controlled by ATR phosphorylation[62]. Consistently, depletion of PCAF in BRCA2-deficient cells, which cannot protect stalled replication forks, promotes PARPi resistance[62]. We speculate that by sequestering PCAF, the delT product could be promoting the PARPi hyper-resistance observed in +/delT cells, a mechanism that could be acting in tumors expressing dominant-negative variants such as c.5946delT.

The fact that +/delT cells maintain similar BRCA2 WT protein levels to the MCF10A suggests a mechanism of homeostatic regulation that requires further investigation. From the number of RNA-seq reads, we estimate that 10-20% of the total BRCA2 mRNA observed corresponds to the mutated allele. The maintained levels of full-length BRCA2 and RAD51 would explain why the DNA repair activity of BRCA2 and DNA damage sensitivity in these cells is not reduced. Importantly, the results obtained with +/del5 cells imply that the HR function of BRCA2 is dosage sensitive, suggesting that any HR hypomorphic mutation in BRCA2 could potentially trigger tumor formation. This idea agrees with the moderate breast cancer susceptibility we reported due to missense hypomorphic variants of *BRCA2*[63]. In contrast, BRCA2 transcriptional regulation activity does not seem to be dosage sensitive, as the +/del5 cells did not show a perturbed transcriptional program.

Despite the lack of HR deficiency in heterozygosity, tumors expressing the delT variant also showed an HRD signature, suggesting that HRD is the predominant driver of tumor progression, as previously described for BRCA1/2-associated tumors[26]. Nonetheless, given that only 2 out of 10 tumors analyzed de novo in this study retained the BRCA2 WT allele, we cannot rule out the possibility that other mutational signatures might arise in other tumors that express the *BRCA2* WT allele. However, a recent report suggests that the accumulation of certain metabolites derived from glycolysis transiently depletes BRCA2 levels; this so-called *induced* haploinsufficiency in cells bearing a monoallelic truncating variant of BRCA2 resulted in mutational patterns related to HRD tumors[28], which could play a role in the HRD signature observed in delT tumors that did not show LOH. Remarkably, LOH status did not change the age at diagnosis in patients bearing either variant, strongly suggesting that inactivation of a single allele is sufficient to promote tumorigenesis as previously suggested[14].

We propose that two different selective processes might be at play in the del5 vs delT scenarios to drive tumorigenesis (Fig. 7d). In c.5946delT, inactivating the WT allele would be an advantage for the tumor to instigate genome instability, which could explain the increase in LOH events observed compared to the tumors harboring the 999del5 variant. This *acquired* genome instability contrasts with the *intrinsic* genome instability present in the case of 999del5, in which the levels of genome instability may already be sufficient to promote tumor formation. In this context, the loss of the second allele might occur as a consequence of genome instability rather than as a requisite for tumorigenesis. Consistent with this idea, only 51% of del5 tumors analyzed presented LOH.

In summary, a common pathogenic truncating variant of BRCA2 uncovers a role for the BRCA2-PCAF complex in NF-κB transcriptional control, which could act as a driver of transformation and invasiveness in *BRCA2*-mutated tumors. Moreover, the collected data on LOH in tumors and the age at diagnosis from patients carrying both variants reinforce the idea that LOH is not a prerequisite for tumorigenesis, consistent with the revised two-hit hypothesis, past and recent work[13,14,28,64]. In support of that idea, a recent study reported epigenetic effects of *Brca1* haploinsufficiency in accelerating tumorigenesis in mouse models, suggesting a single allele primes tumor formation in *BRCA1*-related tumors[65].

Finally, our findings demonstrate that the phenotypic outcome of different *BRCA2* pathogenic variants, as exemplified by c.5946delT and 999del5, is not equivalent, and confirms that haploinsufficiency occurs in the *BRCA2*-mutated context at least when the protein is not produced. These results may have important clinical implications as pathogenic variants are treated equally in the clinic. Based on our

https://doi.org/10.1038/s41467-025-67209-2

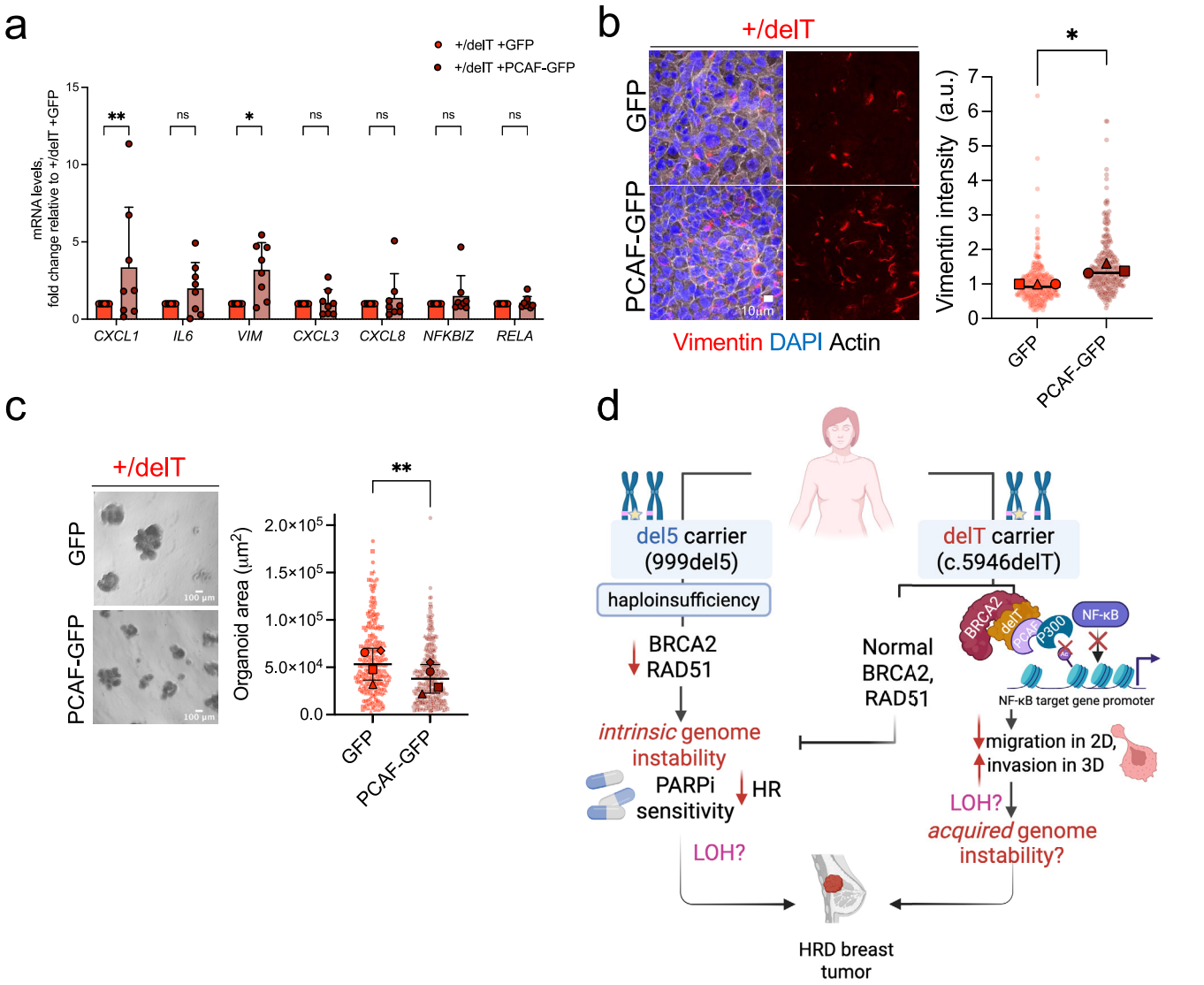

Fig. 7 | PCAF overexpression partially restores NF-κB target gene expression and suppresses invasive features in +/delT cells. a RT-qPCR analysis of NF-κB-regulated genes (*CXCL1, IL6, VIM, CXCL3, CXCL8, NFKBIZ*) and *RELA* in +/delT cells transfected with GFP or PCAF-GFP. Expression was normalized to *PPIA* and shown as fold-change relative to GFP-transfected +/delT cells (n = 8). Data are represented as mean ± SD. Statistical analysis by two-way ANOVA with Šídák's multiple comparisons test; **p = 0.0059, *p = 0.0123, ns > 0.05. **b** (Left) Representative immunofluorescence images of GFP- or PCAF-GFP-transfected +/delT cells stained for vimentin (red), actin (white), and DAPI (blue). Scale bar, 10 µm. (Right) Quantification of vimentin intensity per cell (n = 3; 30 cells/field). The horizontal line represents the median (no error bars). Statistical analysis by two-tailed unpaired t-test with Welch's correction; *p = 0.037. **c** (Left) Brightfield images of organoids derived from GFP- or PCAF-GFP-transfected +/delT cells at day 12. (Right) Quantification of organoid area (n = 4). Data are represented as mean ± SD. Statistical analysis by two-tailed paired t-test; p = 0.0083. All experiments in (**a**-**c**) used clone #1 of +/delT. **d** Working model of early tumorigenic processes in BRCA2 mutation carriers. Left: +/del5 cells show reduced BRCA2 and RAD51 levels, leading to genomic instability, PARPi sensitivity, and HR defects. Right: +/delT cells maintain BRCA2 and RAD51 levels but exhibit altered migration and invasion linked to NF-κB transcriptional rewiring. The truncated delT product sequesters PCAF (and probably P300), reducing H4 acetylation and limiting NF-κB chromatin access. Tumorigenesis may proceed via epigenetic and transcriptomic reprogramming of epithelial proliferation genes, as it was also observed in tumors expressing the delT variant and not those expressing the del5 variant. LOH may occur variably and may be selected for in delT tumors to acquire genome instability, both resulting in HRD mutational signatures. Created in BioRender.com https://BioRender.com/y64b831. Source data are provided as a Source Data file.

results, we predict that carriers of the del5 variant might suffer from higher toxicity to healthy tissue when treated with PARPi. In contrast, delT carriers might benefit from PARPi as a prophylactic measure, as the +/delT healthy tissue would not be sensitive to the drug. Moreover, although direct evidence of dominant negative BRCA2 activity in human tumors remains limited, our findings raise the possibility that some *BRCA2*-mutated cancers may harbor functionally disruptive alleles that actively impair the residual activity of the wild-type protein, with implications for therapeutic response and biomarker interpretation.

Methods

Cell lines

MCF10A cells, kindly provided by Marie Dutreix Lab (Institut Curie, FR), were grown in DMEM-HG/F-12 (Biowest) supplemented with 5% horse serum (Thermo Fisher Scientific), 20 ng/ml human epidermal growth factor (Sigma-Aldrich), 0.5 mg/ml hydrocortisone (Sigma-Aldrich), 100 ng/ml cholera toxin (Sigma-Aldrich), 10 µg/ml insulin (Sigma-Aldrich), and 1% penicillin-streptomycin (Thermo Fisher). MCF7 (kindly provided by Patricia Uguen, Institut Curie, FR) and HEK293T cells (kind gift from Dr. Mounira Amor-Gueret's lab) were

cultured using DMEM (HIMEDIA) supplemented with 10% FBS (EuroBio Abcys) and 1% L-Glutamine (EuroBio Abcys). CAPAN1 cells were obtained from Dr. Ana M. Pizarro (IMDEA Nanociencia, SP) and were grown in the same conditions as MCF7, supplemented with 20% FBS. All cells were regularly tested for mycoplasma contamination.

Generation of BRCA2 gene-edited clones

+/del5 and +/revdel5 were obtained using CRISPR/Cas9- gene editing. 2 μg for each of the following plasmids were used: pCas9-GFP (Addgene # 44719), target sequences cloned in pAC326 containing the pBS U6 sgRNA CRISPR (Addgene # 43860) expressing a reporter mCherry. The homology sequence was introduced by transfecting a single-stranded oligonucleotide (oAC513 or oAC994, Supplementary Data 5) containing the mutation flanked by homology arms to the endogenous BRCA2 region where the mutated base is located, modified with a phosphorothioate linkage (Sigma-Aldrich), and PAGE-purified. From the same screen, we obtained two other clones with 999del2 and 999del4 mutations that, although not equal, the first leads to the same premature stop codon, only keeping one amino acid more, and the second results in a premature stop codon 40 aa downstream of the mutation instead of 17 (Supplementary Fig. 1a).

+/delT was obtained using 5 μg of each TALEN encoding plasmid (TALEN-5′ #V35620 and TALEN-3′ #V35820, Life Technologies) and 1 μg of double-strand oligonucleotide comprising the delT mutation flanked with homology arms obtained by PCR from CAPAN-1 genomic DNA. Two more clones were obtained from the same screen bearing the same mutation (Supplementary Fig. 1a), +/revdelT cells were obtained using CRISPR by transfecting 2 μg of the following plasmids: Cas9-GFP (Addgene #44719) and pU6-pegRNA-GG-acceptor (Addgene#132777), containing the target sequence and the homology sequence. The oligonucleotides and plasmids used for the generation of these clones are listed in Supplementary Data 5 and Supplementary Table 1, respectively.

Cells were transfected using nucleofection (AMAXA technology, Lonza) using nucleofector kit T and the program T024 according to manufacturer instructions. The day after transfection, the medium was changed, and 48 h post-transfection, the cells were trypsinized. Individual GFP-mCherry double-positive cells were sorted using a BD FACSAria III (BD Bioscience) into 96-well plates containing a complete culture medium. Single-cell-derived colonies were gradually expanded and screened for mutations in the two alleles using targeted PCR and the primers listed in Supplementary Data 5.

RNA extraction, RNA-seq, and analysis

2×10^6 cells were harvested, and RNA was isolated using the NucleoSpin Triprep kit (Macherey-Nagel). Before sequencing, RNA integrity and purity were verified through BioAnalyzer RNA 6000 Nano (Agilent) and Nanodrop. RNA libraries were prepared using standard Illumina protocols suitable for strand-specific RNA sequencing. Briefly, a first step of polyA selection using magnetic beads is done to focus sequencing on polyadenylated transcripts. After fragmentation, cDNA synthesis was performed, and the resulting fragments were used for dA-tailing and ligation to indexed adapters (barcodes associated with each sample are included in Supplementary Table 2). PCR amplification was finally achieved to create the final cDNA library. Equimolar pooling of libraries was performed following qPCR quantification using the KAPA Library Quantification Kit (Roche). Sequencing was carried out at the Institut Curie NGS platform using either the TruSeq Stranded mRNA kit on the Illumina HiSeq 2000 system or the Stranded mRNA Prep Ligation kit on the NovaSeq 6000 system, generating 100 bp paired-end FASTQ files.

Raw data sequencing data were processed using the Institut Curie RNA-seq pipeline [https://doi.org/10.5281/zenodo.7446922]. Read quality was assessed using FastQC (v0.11.8 and v0.11.9), and strand specificity was evaluated using RSeQC (v2.6.4 and v4.0.0). Reads were first aligned to a ribosomal RNA reference using Bowtie (v1.2.3 and v1.3.0), followed by alignment to the human reference genome (hg19) using STAR (v2.6.1a and v2.7.6a). Gene-level quantification was performed using STAR's quantMode GeneCounts option with the Gencode v19 annotation. Only protein-coding genes located on autosomes and the X chromosome were retained for downstream analysis. Raw counts were normalized using the TMM method implemented in EdgeR (v3.38.2) and Limma (v3.52.2) within R (v4.2.1, R Core team). Genes with near-zero expression were filtered out. Principal Component Analysis (PCA) was performed using FactoMineR (v2.6), and heatmaps were generated using pheatmap (v1.0.12). Differential expression analysis was conducted using a linear model accounting for sample type, with thresholds set at an adjusted p-value <0.05 and a $\log_2$ fold change >1.5. Gene set enrichment analysis was performed using clusterProfiler (v4.4.4).

Tumor samples were collected retrospectively following informed consent from patients and are available through the Biological Resources Center (CRB) of Institut Curie. RNA from c.5946delT tumors and matched adjacent tissue was extracted using standard protocols. Briefly, DNA was isolated via ethanol/chloroform extraction after tissue dissociation, and RNA was extracted using Qiazol reagent followed by purification with the myRNeasy kit (Qiagen).

RNA-seq data from 999del5 tumors and matched controls were obtained from the European Genome-phenome Archive (EGA) as referenced 46. All tumor RNA-seq datasets were processed using the same analytical pipeline described for the cell clone analyses.

NFKB p536 pathways: The NFKB p536-regulated genes were split into subsets according to their function:

RELA_TARGETS_INFLAMMATORY: IL6, IL8, CXCL1, CXCL2, CXCL3, CCL2, CCL5, TNFAIP3, TNFAIP8, NFKBIA, IL1A, IL1B, PTGS2, NOS2
RELA_TARGETS_IMMUNE_COSTIM: CD40, CD80, CD86, FAS, BIRC3, LTA, LTB, CD44
RELA_TARGETS_MATRIX_INVASION: MMP1, MMP3, MMP9, ICAM1, VCAM1

Differentially expressed genes were identified from normalized RNA-seq data using a $\log_2$ fold-change threshold of 1.5 and an adjusted *p*-value cutoff of 0.05. Analyses were performed in R (v4.2.1) using the edgeR (v3.38.2) and limma-voom (v3.52.2) packages. Gene Set Enrichment Analysis (GSEA) was carried out using the fgsea package (v1.22.0) ranking genes by the product of the fold-change sign and $-\log_{10}$(p-value). An exact Fisher's test was used to assess differences in deregulated Gene Ontology (GO) Biological Processes between del5 and delT tumors. Pearson correlations between the number of differentially expressed genes and deregulated GO terms across tumor and cell samples were computed and visualized using smplot2 (v0.2.5) in R (v4.4.1).

RT-qPCR

Approximately 1×10^6 cells were harvested, and RNA was isolated using the NucleoSpin Triprep kit (Macherey-Nagel). After quantifying the total RNA using Nanodrop, equal amounts of RNA were reverse-transcribed to cDNA using iScript™ Advanced cDNA Synthesis kit (Bio-Rad). Then, the diluted cDNA was used to measure the expression of the respective genes in the CFX Opus Real-Time PCR system (Bio-Rad) using FastStart Universal SYBR Green Master (Merck). The relative mRNA levels were estimated as follows: $2^{(\text{Ct reference} - \text{Ct sample})}$, where Ct reference and Ct sample are mean threshold cycles of RT-qPCR performed in duplicate or triplicate of the reference *(PPIA* and *U6snRNA)* and the gene of interest (sample). The primers used for amplification of respective loci are included in Supplementary Data 5.

Cell proliferation assay with Incucyte System

5×10^3 cells of MCF10A WT and BRCA2-mutated cells were seeded in triplicate in 24-well culture plates (Falcon/Corning). Cells were then incubated for 8 h at 37 °C in a humidified chamber to adhere to the culture plate. Cell growth was imaged every 3 h over 7 days using the Incucyte System (Sartorius). The software calculates the % of confluence covered by cells at each time point. The proliferation rate was calculated from the interpolation of the logistic growth curve obtained in four independent experiments.

Actin staining and circularity score

Confluent MCF10A cells seeded in coverslips inside of P24 plates were fixed with Paraformaldehyde 4% (Electron Microscopy Science) for 15 min at RT. After washing with PBS, they were permeabilized with 0.1% Triton X (Fisher Scientific) in PBS for 10 min and then blocked in 2% BSA (Sigma-Aldrich) in PBS for 30 min. Primary antibodies were diluted into a blocking medium (2% BSA in PBS) and incubated overnight. The day after, coverslips were washed trice with PBS, and incubated with the appropriate 2^{ary} antibodies in a humidity chamber at 37 °C for 1 h. The coverslips were washed 3 times with PBS and mounted with glass prolong mounting media (Thermo Fisher).

Images were acquired with a 63× objective in an LSM800 Inverted Confocal Microscope (Zeiss) and analyzed using ImageJ software. To quantify actin intensity, a region of interest (ROI) was delineated around the perimeter of each cell, and the mean fluorescent pixel intensity was measured. With the same ROIs, the circularity score (4π*area/perimeter^2) was calculated using the shape descriptor tool from ImageJ. Values are from 0 to 1, with a value of 1.0 indicating a perfect circle.

Wound-healing assay

MCF10A cells were grown in P96 wells until confluence and then serum-starved for 24 h. Then, a scratch was performed in the middle of the well with a 10 μl pipette tip. Cell debris was removed by two washes with PBS 1X, and then cells were released in DMEM/F12 media supplemented with 2% horse serum to limit proliferation and incubated further at 37 °C. Bright-field images (Supplementary Fig. 5c) were taken at that moment (time 0) and after 16 h with a Leica Flexicam C1 camera. Wound size was calculated in imageJ by drawing 3 lines at the top, middle, and bottom of the wound image. Migration was calculated as the ratio of the average size of the wound at the endpoint (t = 16 h) compared to the initial time point (t = 0 h). Immunofluorescence images were taken at the endpoint with an LSM800 Inverted Confocal Microscope (Zeiss) and processed with ImageJ software to generate a maximal intensity projection.

Transformation by soft-agar assay

1×10^4 MCF10A cells were suspended in a top layer of DMEM-F12 supplemented media containing 0.30% agar (Sigma) and plated on a bottom layer of DMEM-F12 supplemented media containing 0.6% agar in 35 mm plates. The cells were additionally supplied with a complete medium every 3 days. After 3 weeks, colonies were stained and fixed with 0.01% crystal violet and 10% ethanol in H_2O. Colonies were imaged with a 10× objective in a DM6000B upright widefield microscope (Leica). For each condition, 20 fields were acquired. Images were quantified using ImageJ. The plugin extended depth of field was used to convert 3D acquisitions to 2D images; subsequently, colony size and circularity were measured using ImageJ version 1.53t.

Organoid handling and growth assessment

1×10^4 MCF10A cells were seeded on top of 250 μl of Cultrex Reduced Growth Factor Basement Membrane Gel (RyD) in P24 well plates in DMEM/F12 media (Gibco) supplemented with L-Glutamine, 1X B27 (Gibco), 10 μg/ml insulin (Merck 11376497001), 20 μg/ml hEGF (Sigma-Aldrich), and 1 μg/ml Hydrocortisone (Sigma-Aldrich). In Fig. 7c, +/delT cells were transfected with GFP or PCAF-GFP plasmids (kind gift from Prof. Kyle Miller) using JetPrime according to the manufacturer's specifications. The day after, cells were detached and 1×10^4 were seeded on top of the Cultrex gel. The media was changed every 2–3 days, images were acquired on day 12 post-seeding, and the organoid area was measured by drawing a line delineating the perimeter of each organoid in ImageJ.

Western blot

Cellular pellet was lysed in lysis buffer (50 mM HEPES pH 7.5, 250 mM NaCl, 5 mM EDTA, 1% NP-40,1 mM DTT, 1 mM PMSF, 1X protease inhibitor cocktail (Roche)) and cells were incubated on ice for 60 min, vortexed every 10 min. Lysates were sonicated (3 times × 5 s) and then centrifuged at 18,000 × *g* for 30 min at 4 °C. The supernatant was transferred to a prechilled Eppendorf tube and stored at −80 °C. For protein electrophoresis, samples were heated in 1x SDS sample buffer for 5 min. At 95 °C, loaded on a stain-free 4–15% SDS gel (Bio-Rad), and migrated at 130 V for 90 min. in running buffer (1x Tris-Glycine, 0.1% SDS). The stain-free gel was visualized using a ChemiDoc camera (Bio-Rad). For transfer, a nitrocellulose membrane (VWR) was pre-equilibrated in a transfer buffer (1x Tris-Glycine, 0.025% SDS, 10% methanol). The proteins were transferred for 2 h at 0.35 A at 4 °C. The membrane was blocked in 5% milk in 1x TBS-T at room temperature for 45 min and then incubated with the respective antibody (see antibodies below) in 5% milk in 1x TBS-T overnight at 4 °C. After extensive washes in TBS-T (3 × 10 min), the membrane was incubated for 1 h with the appropriate secondary HRP-antibody at room temperature on a shaker. After three more washes in TBS-T, the membrane was developed using ECL Prime Western Blotting Detection Reagent (VWR) and visualized using a chemiluminescence imaging system, either ChemiDoc Camera (BIO-RAD) or Amersham Imager 680.

Subcellular fractionation

For Supplementary Fig. 6a, 1×10^7 MCF10A cells were trypsinized, pelleted, and incubated on ice for 20 min with 500 μl of BAD buffer (10 mM HEPES pH 7.9, 10 mM KCl, 10% glycerol, 1.5 mM $MgCl_2$, 0.34 M sucrose, 1 mM DTT, 0.1 mM PMSF, 1X protease inhibitor cocktail (EDTA-free, Roche)) complemented with 0.1% Triton X-100. After collecting 20 μl of total cell lysate, the pellets were centrifuged at 1300 × *g* for 5 min at 4 °C. The supernatant, containing the cytoplasmic fraction, was transferred to a prechilled tube. Pellets containing the chromatin fraction were then washed twice with 1.5 ml BAD buffer and centrifuged at 1300 × *g* for 5 min at 4 °C. Finally, the pellets were incubated in 500 μl of lysis buffer (50 mM HEPES pH 7.5, 250 mM NaCl, 5 mM EDTA, 1% NP-40, 1 mM DTT, 1 mM PMSF, 1x protease inhibitor cocktail (EDTA-free, Roche)) for 40 min. Protein samples were subsequently boiled in 1X Laemmli buffer at 95 °C for 5 min, separated on 4–15% SDS-PAGE precast protein gels (BIO-RAD), and analyzed by western blot.

The subcellular fractionation in Fig. 6b and Supplementary Fig. 7a was performed as follows: MCF10A (WT, +/delT) and CAPAN-1 cells from an 80% confluent 60 mm culture dish were pelleted, resuspended in 1 ml of buffer 1 (10 mM Tris pH 7.4, 10 mM NaCl, 3 mM $MgCl_2$), and centrifuged at 2500 × *g* for 5 min at 4 °C. The cell pellets were incubated with 200 μl of buffer 2 (10 mM Tris 1 M pH 7.4, 10 mM NaCl, 3 mM $MgCl_2$, 10% Glycerol, 0.5% NP-40, 0.5 mM DTT, 1X protease inhibitor cocktail (EDTA-free; Roche) for 3 min and centrifuged at 5250 × *g* for 5 min at 4 °C. The supernatant was collected in a new tube (cytoplasmic fraction), and the pellet was resuspended in 250 μl lysis buffer (50 mM HEPES pH 7.5, 1 mM DTT, 1 mM $MgCl_2$, 150 mM NaCl, 1% NP-40, 0.1% Triton X-100, 100U Benzonase, and 1X protease inhibitor cocktail (EDTA-free; Roche)) and lysed for 30 min on ice in a new tube. The nuclear lysates were further sonicated once at 50 amplitudes for 20 s. using a probe sonicator (Sonics & Materials, Inc.). Protein samples were then prepared as above for the Western blot.

Antibodies for Western blot and immunofluorescence

Mouse anti-BRCA2 (1:500, OP95, EMD Millipore), rabbit anti-N-ter-BRCA2 (raised for this study using BRCA2 aa 188-563 as antigen; 1:1000, GenScript), rabbit anti-C-ter-BRCA2 (1:1000, Bethly Laboratories), rabbit anti-RAD51 (1:2000, Abcam), mouse anti-alpha Tubulin (1:5000, Euromedex), rabbit anti-histone H3 (1:2000, Euromedex), rat anti-Vimentin (1:1000, MAB2105, RyD), mouse anti-histone H4 total (1:1000 Cell Signaling), (rabbit anti-histone H4 (acetyl K5 + K8 + K12 + K16)(abcam,1:5000), mouse anti-Ki67 (1:2000, 8D5, Cell Signaling), mouse anti-NF-kB p65 (1:1000, Cell Signaling Technology), rabbit anti-NF-kB p65 (phospho S536, 1:2000, abcam). Mouse anti-PCAF (1:500, Santa Cruz), rabbit anti-PCAF (1:1000, Selleck Chemicals), rabbit anti-P300 (1:1000, Cell Signaling Technology), mouse anti-GFP (1:1000, Roche, 11814460001), rabbit anti-RFP (1:1000, Enzo, AB233). Secondary antibodies: Horseradish peroxidase (HRP) conjugated secondary antibodies used: goat anti-mouse IgG-HRP (1:10,000, Jackson ImmunoResearch), goat anti-rabbit IgG-HRP (1:10,000, Jackson ImmunoResearch), IRDye® 680RD Anti-IgG Goat Secondary Antibody (1:20,000, LICORbio), and IRDye® 800CW Anti-Rabbit IgG Goat Secondary Antibody (1:20,000, LICORbio). Alexa Fluor 488 Donkey anti-Mouse IgG (H + L) (1:500, Thermo Fisher A-21202), Alexa Fluor 594 Donkey anti-Rat IgG (1:500, Thermo Fisher A-21209), DAPI (Merck 508741).

Plasmid transfection and RNAi silencing

siRNA transfections were performed in a serum-containing medium with the transfection reagent JetPrime (Ozyme) or Lipofectamine RNAiMax (Thermo Fisher Scientific Inc.) following the manufacturer's instructions. For BRCA2 silencing, we transfected BRCA2 siRNA (Dharmacon D-003462-0, GAAGAAUGCAGGUUUAAUA, 20–50 nM). The non-targeting siRNA #4 (Dharmacon D-001810-04-20, 20-50 nM) was used as a control (siCTRL) in the cells. Experiments were performed 48 h after transfection.

PCAF-GFP plasmid and GFP control vector (kind gift from Prof. Kyle Miller) were transfected using TurboFect™ (Thermo Fisher Scientific Inc.) or JetPrime (Ozyme) using a reverse transfection protocol per the manufacturer's instructions. Experiments were performed 6 days after a single round of transfection.

Immunoprecipitation

Endogenous full-length or truncated BRCA2 was immunoprecipitated from MCF10A, +/delT, HEK293T, or CAPAN-1 cells as follows: For MCF10A, cell pellets were resuspended in 1 ml Buffer 1 (10 mM Tris pH 7.4, 10 mM NaCl, 3 mM $MgCl_2$) and incubated on ice for 1 min, followed by centrifugation at 2500 × *g* for 5 min. The pellets containing the nuclear fractions were resuspended in 100-200 µl of Buffer 2 (10 mM Tris 1 M pH 7.4, 10 mM NaCl, 3 mM $MgCl_2$, 10% Glycerol, 0.5% NP-40, 0.5 mM DTT) and centrifuged at 5250 × *g* for 5 min. The pellets were then lysed in 1 ml lysis buffer (50 mM HEPES, pH 7.5, 1 mM DTT, 1 mM $MgCl_2$, 150 mM NaCl, 1% NP-40, 0.1% Triton X-100, 250U Benzonase, and 1X protease inhibitor cocktail (Complete, EDTA-free; Roche)) for 30 min at 4 °C under rotation. For CAPAN-1 and HEK293T, total cell lysates were used; cell pellets were lysed in 1 ml of lysis buffer for at least 30 min at 4 °C under rotation. After clearing the lysates by centrifugation at 16,000 × *g* for 15 min, they were divided into two halves. One half was incubated with 5 µg of BRCA2 antibody (BRCA2 N-terminal (in-house)) and the other with 5 µg rabbit IgG (Thermo Fisher Scientific, 02-6102) overnight under rotation at 4 °C. In HEK293T cells, 3 µg each of BRCA2 (C-terminal) and rabbit IgG antibodies were used. BRCA2 complexes were captured using 50 µl Dynabeads Protein G (Life Technologies) for 2 h under rotation at 4 °C. The beads were collected using a magnet and washed five times with wash buffer 1 (50 mM HEPES pH 7.5, 1 mM $MgCl_2$, 250 mM NaCl, 1% NP-40, and 0.1% Triton X-100) in the case of the MCF10A and HEK293T, or once with wash buffer 1 and once with wash buffer 2 (50 mM HEPES pH 7.5, 1 mM $MgCl_2$, 500 mM NaCl, 1% NP-40, and 0.1% Triton X-100) in the case of CAPAN-1 cells. Protein complexes were eluted by boiling the beads in 2X Laemmli buffer, separated by 4–15% SDS-PAGE precast protein gels (BIO-RAD), and analyzed by western blot.

GFP-TRAP

A 10-cm plate of HEK293T cells was transiently transfected with the following plasmids: GFP-MBP-NLS (2.5 µg), GFP-MBP-BRCA2 (WT or the delT) together with MBP-BRCA2-WT-RFP (5 µg each), as indicated in the legend, using Turbofect following the manufacturer's specifications. For the GFP-Traps in Supplementary Fig. 7d, a 15-cm plate of HEK293T was transfected with either GFP-MBP-NLS (2.5 µg) or GFP-MBP-BRCA2 (20 µg). 36 h later, cells were collected and lysed in co-IP lysis buffer (50 mM HEPES pH 7.5, 1 mM DTT, 1 mM $MgCl_2$, 150 mM NaCl, 1% NP-40, 0.1% Triton X-100, including 1x protease inhibitor cocktail (EDTA-free) and 250 U Benzonase. Samples were incubated for 30 min at 4 °C under rotation. Total protein in the lysates was quantified by Bradford assay. A 50 µg input sample was collected in a separate tube and mixed with 3x Laemmli buffer. The samples were cleared by centrifugation at 20,000 × *g* for 15 min, and the cleared lysates were subjected to GFP pull-down with 25 µl of GFP-Trap beads (Chromotek) for 90 min at 4 °C under rotation. The beads were then washed thrice with wash buffer (50 mM HEPES pH 7.5, 1 mM $MgCl_2$, 250 mM NaCl, 1% NP-40, and 0.1% Triton X-100) and boiled for 5 min at 95 °C in 2x Laemmli buffer along with the input samples. Proteins were separated in SDS-PAGE 4-15% precast gels (BIO-RAD) and analyzed by western blot using either Odyssey Infrared Imaging System (Licor; V3.0) or ECL Amersham Imager 680.

PARPi, MMC, and HU sensitivity assessed by MTT assay

Cell viability was assessed in MCF10A parental cells or MCF10A BRCA2-mutated clones using MCF10A transfected with either siCTRL or siBRCA2 as controls, as indicated in the legends.

Olaparib (AZD2281, Selleck Chemicals): Cells were seeded in triplicate in 96-well plates (TPP). The following day, they were treated at increasing concentrations of the drug (0.5, 1.0, and 2.5 µM) for 6 days. MMC (Sigma-Aldrich) and HU (Sigma-Aldrich): 3×10^5 cells were seeded in a 6-well plate (TPP). For MMC, cells were treated for one hour with the following concentrations of the drug: 0, 1.0, 2.0, and 4.0 µM. For HU, cells were treated for 24 h with the following concentrations of the drug: 0, 2.5, and 5 mM. Subsequently, cells were harvested and seeded in triplicate in 96-well plates. On the 6th day, the media was removed and cells were washed with 1x PBS. Cell viability was assessed with 3-[4,5-Dimethylthiazol-2-yl]−2,5-diphenyltetrazolium bromide (MTT, #M5655, Sigma Aldrich). The solution was removed, and MTT crystals were dissolved in 100 µl 100% DMSO (Sigma-Aldrich). The absorbance was obtained from the Tristar 3 microplate reader (Berthold Technologies) at 570 nm. The relative surviving cells were calculated by dividing the absorbance of the treated cells by the absorbance obtained in the untreated condition of the same clone.

In the case of the EGF survival assay (Supplementary Fig. 6c), 2000 MCF10A and +/delT cells were seeded in 96-well plates in MCF10A normal media (containing 20 ng/ml EGF) or in the same media without EGF. After 72 h incubation at 37 °C, cell viability was assessed as above using a FLUOstar OPTIMA microplate reader (BMG Labtech). The relative surviving cells were normalized against the MCF10A parental cell line in conditions of normal media (+EGF).

Clonogenic survival to assess sensitivity to HU

Cells seeded at 70% of confluence in a 6-well plate were treated with HU (Sigma-Aldrich) at concentrations of 0, 2.5, 5, or 10 mM. After 24 h treatment, the cells were serially diluted in complete growth media (Eurobio) and seeded at 500, 1000, 2000, and 4000 cells in triplicate in 60 mm dishes depending on the drug concentration. The media was changed every third day. After 14 days in culture, the plates were stained with crystal violet (Sigma-Aldrich), colonies were counted, and

the surviving fraction was determined by calculating it as the ratio of the number of colonies formed to the total number of cells plated.

Cell-based homologous recombination assay

2.5×10^6 cells for control, 3×10^6 for BRCA2-mutated clones, were seeded in 10 cm plates. The following day, cells were detached and counted. 1×10^6 cells were mixed in a total amount of 400 µl of Opti-mem (Gibco) with 5 µg of each of these three plasmids: spCas9-GFP, AAVS1-gRNA, and the plasmid coding for the mCherry protein flanked with two regions of homology for the AAVS1 site. For control cells, the AAVS1-gRNA (gRNA) plasmid was excluded from the mix. Cells were electroporated in a 0.4 µm cuvette with a Gene Pulser (BioRad) at 350 V and 960 µF, and seeded into a P6 well plate. 2 days later, cells were detached and GFP+ cells (expressing spCas9) were sorted using FACS-Aria Fusion Sorting Cytometer. The same number of GFP+ sorted cells was seeded for each condition. 6 days after (8 days from electroporation), the percentage of mCherry+ cells was quantified using a FACS-Aria Fusion Cytometer. The oligonucleotides with the target sequence used for the CRISPR are indicated in Supplementary Data 5.

DNA combing assay with S1 treatment to assess PARPi-induced ssDNA gaps

Cells were seeded in a 10 cm plate and allowed to adhere for 24 h (2×10^6 cells for control, 3.5×10^6 for BRCA2-mutated clones). The following day, DNA was labeled for 30 min with 100 µM IdU (Sigma-Aldrich) and washed twice with PBS, followed by simultaneous incubation for 2 h with 100 µM CIdU (Sigma-Aldrich) and 30 µM Olaparib (AZD2281, Selleck Chemicals). After labeling, cells were washed twice with PBS and permeabilized with 5 ml CSK buffer in a 10 cm dish (10 mM PIPES, pH 6.8, 0.1 M NaCl, 0.3 M sucrose, 3 mM $MgCl_2$, EDTA-free Protease Inhibitor Cocktail (Roche)) at room temperature for 10 min. Subsequently, cells were incubated with 1 ml of S1 buffer (30 mM sodium acetate, pH 4.6, 1 mM zinc sulfate, 50 mM NaCl) was added with or without S1 nuclease (20 U) (Thermofisher # 18001016) for 30 min at 37 °C. Finally, cells were collected by scraping, pelleted, and resuspended in PBS (45 µl per 400,000 cells).

500 µl of cells were transferred to a new tube, briefly heated at 42 °C, and resuspended with 500 µl melted 2% agarose type VII (SIGMA) to make the agarose plugs. Plugs were left to solidify for 20 min at 4 °C and were then digested with Proteinase K (400 mM EDTA pH 8, 10% Proteinase K, 1% Sarcosyl) in a water bath at 42 °C overnight. The next day, the plugs were washed trice with TE 1X buffer. TE solution was removed, and a solution containing 50 mM MES pH 5.5, 100 mM NaCl was added to the plugs that were heated at 68 °C for 20 min. Agarose plugs were then dissolved by adding 2 µl of β-agarase (NEB) and incubated at 42 °C overnight. The following day, dissolved agarose plugs were transferred to the combing machine (Genomic Vision), where DNA was combed onto silane-coated coverslips (Genomic Vision COV-002-RUO) following the manufacturer's specifications. Combed coverslips were baked overnight at 60 °C, denatured in denaturation buffer (25 mM NaOH, 200 mM NaCl in H2O) for 15 min, washed thrice with 1X PBS, and dehydrated by incubation with increasing concentrations of ethanol 70%, 90%, and 100% each for 5 min. For the IF staining, the coverslips were incubated with BlockAid for 15 min (Life Technologies) at RT, followed by the primary anti-IdU and anti-CldU antibodies (1 h, 1:25 anti-mouse Becton Dickinson 347580 for IdU and 1:50 anti-rat Abcam ab6326 for CldU) and then incubated 1 h with the following secondary antibodies: 1:50 Alexa donkey anti-mouse 488 (Life Technologies ref. 21202), 1:50 Alexa goat anti-rat 555 (Life Technologies ref. A21434) in BlockAid (Thermo Scientific). Slides were air-dried for 5–10 min and were mounted with 7 µl mounting media (80% Glycerol and 20% PBS) and sealed with clear nail polish. Track lengths were measured in Fiji, and the ratio was calculated by dividing the IdU (green) by the CldU (red) signal.

Metaphase spreads

12,500 MCF10A cells were seeded into glass coverslips in P24 wells. The day after, cells were treated with 10 µM of Olaparib for another 24 h. Cell division was blocked with 100 ng/ml colcemid (Thermo Fisher) for 3 h. Then, a hypotonic shock was performed with 1:7 FBS in distilled water for 40 min. After which the cells were fixed by adding 1 volume of 3:1 Methanol-Acetic Acid for 15 min at RT, then exchanged with 3:1 Methanol-acetic acid for 15 min at RT and then for 30 min at 4 °C. Coverslips were air-dried and stained with 2% Giemsa solution (Thermo Fisher) diluted in Gurr buffer (Thermo Fisher) for 10 min. The coverslips were rinsed in water and air-dried at RT, then mounted with Eukitt mounting media (Sigma-Aldrich). Images were acquired with a 100X objective with a CMOS camera (LEICA).

Cell cycle analysis by flow cytometry

1×10^6 cells were harvested and washed twice with PBS. Cells were then fixed in ice-cold 70% ethanol overnight, before being pelleted, resuspended in ice-cold PBS, and then incubated in the dark in propidium iodide (PI) staining buffer (3.5 mM Tris HCl, pH 7.6, 50 µg/ml PI, 50 µg/ml RNase A, 0.1% NP-40, 10 mM NaCl, ddH20) for 30 min at room temperature. Cell cycle distribution was analyzed by flow cytometry BD FACSAria III (BD Bioscience) using the FACSDiva software, and data were analyzed with the FlowJo 10.5 software (Tree Star Inc.).

γH2AX and RAD51 immunofluorescence staining and quantitative image-based cytometry (QIBC)

Cell treatments: MCF10A WT, +/delT, and +/del5 cells were treated with DMSO as a control, 10 µM PARPi olaparib (Selleckchem, S1060), or 3 µM mitomycin C (Sigma-Aldrich, M7949) for 24 h as indicated.

Immunofluorescence staining: Cells were grown on µ-Plate 96-well plates (ibidi, 89626), fixed in 3% formaldehyde in PBS for 15 min at RT, washed twice in PBS, permeabilized for 5 min at room temperature in 0.2% Triton X-100 (Sigma-Aldrich) in PBS, and washed twice in PBS. Primary and secondary antibodies were diluted in filtered DMEM containing 10% FBS and 0.02% sodium azide. Incubations in primary and secondary antibodies were performed at room temperature for 2 h and 1 h, respectively, with three washes in PBS in between. Cells were then washed once with PBS and incubated for 10 min at room temperature with PBS containing 4′,6-diamidino-2-phenylindole dihydrochloride (DAPI, 0.5 µg/ml) to stain DNA. Cells were subsequently washed three times in PBS before imaging. The following primary antibodies were used: RAD51 (rabbit, Bioacademia 70-002, 1:1000), H2AX Phospho S139 (mouse, Biolegend 613401, 1:1000). Secondary antibodies were: Alexa Fluor 488 Goat Anti-Rabbit (Life Technologies, A11034, 1:500), Alexa Fluor 568 Goat Anti-Mouse (Life Technologies, A11031, 1:500).

Automated multichannel widefield microscopy for quantitative image-based cytometry (QIBC) was performed as described previously[66,67] on an Olympus ScanR Screening System (ScanR Image Acquisition 3.01) equipped with an inverted motorized Olympus IX83 microscope, a motorized stage, IR-laser hardware autofocus, a fast emission filter wheel with one set of bandpass filters for multi-wavelength acquisition (DAPI (ex BP 395/25, em BP 435/26), FITC (ex BP 470/24, em BP 511/23), TRITC (ex BP 550/15, em BP 595/40), Cy5 (ex BP 640/30, em BP 705/72)), and a Hamamatsu ORCA-FLASH 4.0 V2 sCMOS camera (2048 × 2048 pixel, pixel size 6.5 × 6.5 µm) with a ×20 UPLSAPO (NA 0.75) air objective. For each condition, image information of large cohorts of cells (typically at least 1000 cells for the UPLSAPO 20× objective (NA 0.75)) was acquired under non-saturating conditions, and identical settings were applied to all samples within one experiment. Images were analyzed with the Olympus ScanR Image Analysis Software (version 3.3.0), a dynamic background correction was applied, and nuclei segmentation was performed using an integrated intensity-based object-detection module based on the DAPI signal. Nuclear foci segmentation was performed using an integrated

spot-detection module. All downstream analyses were focused on properly detected interphase nuclei containing a 2N-4N DNA content as measured by total and mean DAPI intensities. Color-coded scatter plots of asynchronous cell populations were generated with Spotfire data visualization software (version 10.10.1.7, TIBCO). Within one experiment, similar cell numbers were compared for the different conditions. For visualization of discrete data in scatter plots, mild jittering (random displacement of data points along the discrete data axes) was applied to demerge overlapping data points. Representative scatter plots and quantifications of independent experiments are shown.

Spheroid invasion assay

Around sixty 20 µl drops containing 3000 cells resuspended in the medium were seeded to form spheroids of MCF10A or +/delT cells by hanging drop method on the underside of a 10 cm petri dish lid. The lid was then inverted over the dish (filled with PBS). 24 h after incubation at 37 °C, drops were carefully collected with a P1000 tip (-150 µl), and mixed 1:1 with a pH-adjusted solution of Collagen type 1 (Corning) to a final concentration of 1.5 mg/ml. The 300 µl mix was seeded in a well of a 24-well plate. After 1 h of incubation at 37 °C, 500 µl of complete media was added on top of the collagen gel. The day after, the spheroids were imaged using a Leica Flexicam C1 camera, and both the area of the spheroid and the area of spheroids+protusions (total spheroid area) were quantified by drawing a line around the limit of the spheroid or the protrusions using ImageJ software. We used the ratio of total area/spheroid area to compare the invasion capacity.

Whole genome sequencing

The internal review boards of each participating institution approved the collection and use of samples from all patients in this study. Informed consent was obtained by the relevant participating institution.

DNA was extracted from both tumor and corresponding normal tissue, and samples were subjected to whole-genome sequencing. The resulting BAM files were aligned to the reference human genome (GRCh37) using the Burrows-Wheeler aligner, BWA (v0.5.9). Mutation calling was performed as described previously[45,46]. Briefly, CaVEMan (Cancer Variants Through Expectation Maximization; http://cancerit.github.io/CaVEMan/) was used to call somatic substitutions. Indels in the tumor and normal genomes were called using modified Pindel (v2.0, http://cancerit.github.io/cgpPindel/) on the NCBI37 genome build. Structural variants were discovered using a bespoke algorithm, BRASS (BReakpoint AnalySiS) (https://github.com/cancerit/BRASS), through discordantly mapping paired-end reads followed by de novo local assembly using Velvet[68] to determine exact coordinates and features of the breakpoint junction sequence.

Lolliplot analysis. Whole Genome Sequencing (WGS) reads (datasets listed in Supplementary Table 2) were aligned to the human reference genome (hg19) using BWA-MEM (v0.7.15). Variant calling of single-nucleotide variants (SNVs) and small insertions/deletions (indels) was performed using the GATK Mutect2 (v4.1.9.0). Post-calling filtering to remove technical artifacts and sequencing errors using the GATK FilterMutectCalls.

Variants located within the coding regions of the BRCA2 gene (NM_000059) were extracted using SnpSift (v5.1), applying thresholds of allelic ratio ≥10% and coverage ≥20×. Visualization of variant distribution across the BRCA2 coding sequence was performed using lolliplots generated in R (v4.2.1) with the packages trackViewer (v1.34.0), VariantAnnotation (v1.44.0), TxDb.Hsapiens.UCSC.hg19.refGene (v0.0.99), and org.Hs.eg.db (v3.15.0).

Extraction of mutational signatures. Mutational signatures analysis was performed following a three-step process as previously described[45]: (i) hierarchical de novo extraction based on somatic substitutions and their immediate sequence context, (ii) updating the set of consensus signatures using the mutational signatures extracted from breast cancer genomes, and (iii) evaluating the contributions of each of the updated consensus signatures in each of the breast cancer samples.

The complete compendium of consensus mutational signatures that were found in our cohort of breast cancers with the two pathogenic variants includes signatures 1, 2, 3, 5, 8, 13, 17, 18, and 127 (Fig. 3, Supplementary Fig. 3).

Mutational signatures that did not contribute large numbers (or proportions) of mutations or that did not significantly improve the correlation between the original mutational pattern of the sample and the one generated by the mutational signatures were excluded from the sample. This procedure reduced the over-fitting of the data and allowed only the essential mutational signatures to be present in each sample.

HRD score. The HRD score determination was conducted using the HRDetect predictor[45], considering the following genomic features, listed in their respective order of importance: deletions with microhomology, substitution signature 3, rearrangement signatures 3 and 5, HRD index, and substitution signature 8. For further details, see ref. 45.

Allele-specific LOH status. For the BRCA2-del5 Icelandic cohort (published + 1 new)[15,17], the proportion of the BRCA2 wild-type (wt) alleles was quantitatively measured relative to the 999del5 BRCA2 mutated alleles in tumor DNA samples by quantitative polymerase chain reaction (qPCR) (7500 Realtime PCR system; Applied Biosystems) with a TaqMan method as previously described[15,17,23]. Briefly, using a single forward primer and two different reverse primers, one designed to amplify the wild-type allele and another for the *BRCA2 999del5* allele, and a FAM-labeled TaqMan probe, the average Ct value was determined by duplicate qPCRs for the two primer pairs in 2 separate reactions. When the *BRCA2* wild-type allele proportion was below 33% the sample was defined as presenting *BRCA2* LOH. Some of these results were further confirmed by array comparative genomic hybridization (aCGH) (Supplementary Data 1).

For the BRCA2-delT Penn cohort (n = 2 + published)[13], a combination of VarScan2[69], allele frequency comparisons, and allele-specific copy number calls was used to determine BRCA locus-specific LOH. Estimates of tumor purity (cellularity) were determined using Sequenza and inputted into VarScan2 variant calling. The sample was assigned a locus-specific LOH positive status if the VarScan2 somatic P-value was significant and a locus-specific LOH negative status if the VarScan2 germline P-value was significant. Allele-specific copy number calls of the genomic region containing the BRCA2 mutation were determined by Sequenza. The copy number of the genomic region surrounding the germline BRCA2 mutation (CN) and the number of mutant (m) alleles as per the output of the Sequenza program were used to assign two states of absent locus-specific LOH—heterozygous diploid (CN = 2;m = 1) or amplified with gain of non-mutant (wildtype) allele (CN > 2;m = 1)—and three states of locus-specific LOH—loss (CN = 1;m = 1), copy neutral LOH (CN = 2; m = 2), and amplified with LOH (CN > 2;m > 2). The genomic regions surrounding the germline BRCA2 mutation ranged from less than one to over 100 Mb in length. In cases where the VarScan2 and ASCN calls differed, the difference between cellularity-corrected tumor allele frequency and blood allele frequency (ΔAF) was determined; the sample was assigned a locus-specific LOH positive status if ΔAF > 0.2028.

For the I. Curie cohort, raw sequences were generated per sample using the PCR Free Roche KAPA Hyper Prep Library on the Illumina Novaseq 6000 (run D458) at the NGS platform of the Institut Curie, resulting in the creation of 150 bp paired-end fastq files. Raw data were then processed using the Institut Curie raw-qc pipeline (10.5281/

zenodo.8340106). The overall quality of the reads was checked using FastQC (v0.11.8). Reads were then aligned on the hg19 reference genome using bwa mem (v.0.7.15). Aligned data were processed using Facets (v0.5.1) that take advantage of both the B-allele ratio (BAF) and the read depth to estimate the allele-specific copy number variants and the optimal ploidy and tumor cellularity, after a GC percentage correction. Total copy number (number of A and B in the genotype) and minor copy number (number of B in the genotype) were defined for each segment. LOH was considered for segments with a minor copy number of 0.

Statistical analysis

Statistical analyses were performed using GraphPad Prism (Version 10.0). Statistical parameters and tests are reported in the figures and corresponding figure legends. The number of samples (n) in figure legends represents independent biological replicates unless stated otherwise. The statistical significance was obtained from the mean of the independent experiments. No statistical methods were used to determine the sample size before starting experiments. For the volcano plots shown in Fig. 4a, b and Supplementary Fig. 4c and the Supplementary Data 1 and 2 the differentially expressed genes were obtained using moderated t-tests (two-sided) and a multiple testing correction was applied (Benjamini-Hochberg) with an adjusted *p*-value threshold of 5%.

Reporting summary

Further information on research design is available in the Nature Portfolio Reporting Summary linked to this article.

Data availability

All materials related to this study are available upon request from the corresponding author. Any further inquiries or requests for resources and reagents should be directed to the corresponding author. The Raw sequence files listed in Supplementary Table 2 have been deposited at the European Genome-Phenome Archive with accession numbers EGAS50000000613 and EGAS50000000614 and to NCBI's Gene Expression Omnibus with the GEO Series accession number GSE272335. Source data are provided with this paper.

References

1. Minello, A. & Carreira, A. BRCA1/2 haploinsufficiency: exploring the impact of losing one allele. *J. Mol. Biol.* **436**, 168277 (2023).
2. Sessa, G. et al. BRCA2 promotes R-loop resolution by DDX5 helicase at DNA breaks to facilitate their repair by homologous recombination. *EMBO J.* **40**, e106018 (2021).
3. Schlacher, K. et al. Double-strand break repair-independent role for BRCA2 in blocking stalled replication fork degradation by MRE11. *Cell* **145**, 529–542 (2011).
4. Lomonosov, M., Anand, S., Sangrithi, M., Davies, R. & Venkitaraman, A. R. Stabilization of stalled DNA replication forks by the BRCA2 breast cancer susceptibility protein. *Gene Dev.* **17**, 3017–3022 (2003).
5. Kolinjivadi, A. M. et al. Smarcal1-mediated fork reversal triggers Mre11-dependent degradation of nascent DNA in the absence of Brca2 and stable Rad51 nucleofilaments. *Mol. Cell* **67**, 867–881.e7 (2017).
6. Panzarino, N. J. et al. Replication gaps underlie BRCA deficiency and therapy response. *Cancer Res.* **81**, 1388–1397 (2021).
7. Quinet, A. et al. PRIMPOL-mediated adaptive response suppresses replication fork reversal in BRCA-deficient cells. *Mol. Cell* **77**, 461–474.e9 (2020).
8. Vugic, D. et al. Replication gap suppression depends on the double-strand DNA-binding activity of BRCA2. *Nat. Commun.* **14**, 446 (2023).
9. Daniels, M. J., Wang, Y., Lee, M. & Venkitaraman, A. R. Abnormal cytokinesis in cells deficient in the breast cancer susceptibility protein BRCA2. *Science* **306**, 876–879 (2004).
10. Mondal, G. et al. BRCA2 localization to the midbody by filamin A regulates cep55 signaling and completion of cytokinesis. *Dev. Cell* **23**, 137–152 (2012).
11. Ehlen, A. et al. Proper chromosome alignment depends on BRCA2 phosphorylation by PLK1. *Nat. Commun.* **11**, 1–21 (2020).
12. Fuks, F., Milner, J. & Kouzarides, T. BRCA2 associates with acetyltransferase activity when bound to P/CAF. *Oncogene* **17**, 2531–2534 (1998).
13. Maxwell, K. N. et al. BRCA locus-specific loss of heterozygosity in germline BRCA1 and BRCA2 carriers. *Nat. Commun.* **8**, 319–11 (2017).
14. King, T. A. et al. Heterogenic loss of the wild-type BRCA allele in human breast tumorigenesis. *Ann. Surg. Oncol.* **14**, 2510–2518 (2007).
15. Stefansson, O. A. et al. Genomic and phenotypic analysis of BRCA2-mutated breast cancers reveals co-occurring changes linked to progression. *Breast Cancer Res.* **13**, R95 (2011).
16. Heetvelde, M. V. et al. Accurate detection and quantification of epigenetic and genetic second hits in BRCA1 and BRCA2-associated hereditary breast and ovarian cancer reveals multiple co-acting second hits. *Cancer Lett.* **425**, 125–133 (2018).
17. Aradottir, M. et al. Aurora A is a prognostic marker for breast cancer arising in BRCA2 mutation carriers. *J. Pathol. Clin. Res.* **1**, 33–40 (2015).
18. Karaayvaz-Yildirim, M. et al. Aneuploidy and a deregulated DNA damage response suggest haploinsufficiency in breast tissues of BRCA2 mutation carriers. *Sci. Adv.* **6**, eaay2611 (2020).
19. Gruber, J. J. et al. Chromatin Remodeling in Response to BRCA2-Crisis. *Cell Rep.* **28**, 2182–2193.e6 (2019).
20. Lim, P. X., Zaman, M., Feng, W. & Jasin, M. BRCA2 promotes genomic integrity and therapy resistance primarily through its role in homology-directed repair. *Mol. Cell* https://doi.org/10.1016/j.molcel.2023.12.025 (2024).
21. Tan, S. L. W. et al. A class of environmental and endogenous toxins induces BRCA2 haploinsufficiency and genome instability. *Cell* **169**, 1105–1118.e15 (2017).
22. Arnold, K. et al. Lower level of BRCA2 protein in heterozygous mutation carriers is correlated with an increase in DNA double strand breaks and an impaired DSB repair. *Cancer Lett.* **243**, 90–100 (2006).
23. Skoulidis, F. et al. Germline Brca2 heterozygosity promotes Kras(G12D) -driven carcinogenesis in a murine model of familial pancreatic cancer. *Cancer Cell* **18**, 499–509 (2010).
24. Bellacosa, A. et al. Altered gene expression in morphologically normal epithelial cells from heterozygous carriers of BRCA1 or BRCA2 mutations. *Cancer Prev. Res.* **3**, 48–61 (2010).
25. Tannenbaum, B., Mofunanya, T. & Schoenfeld, A. R. DNA damage repair is unaffected by mimicked heterozygous levels of BRCA2 in HT-29 cells. *Int. J. Biol. Sci.* **3**, 402–407 (2007).
26. Warren, M., Lord, C. J., Masabanda, J., Griffin, D. & Ashworth, A. Phenotypic effects of heterozygosity for a BRCA2 mutation. *Hum. Mol. Genet.* **12**, 2645–2656 (2003).
27. Kim, M.-K. et al. Increased rates of spontaneous sister chromatid exchange in lymphocytes of BRCA2+/- carriers of familial breast cancer clusters. *Cancer Lett.* **210**, 85–94 (2004).
28. Kong, L. R. et al. A glycolytic metabolite bypasses "two-hit" tumor suppression by BRCA2. *Cell* https://doi.org/10.1016/j.cell.2024.03.006 (2024).
29. Rebbeck, T. R. et al. Association of type and location of BRCA1 and BRCA2 mutations with risk of breast and ovarian cancer. *Jama* **313**, 1347–1361 (2015).
30. Ware, M. D. et al. Does nonsense-mediated mRNA decay explain the ovarian cancer cluster region of the BRCA2 gene?. *Oncogene* **25**, 323–328 (2006).
31. Berman, D. B. et al. A common mutation in BRCA2 that predisposes to a variety of cancers is found in both Jewish Ashkenazi and non-Jewish individuals. *Cancer Res.* **56**, 3409–3414 (1996).

32. Neuhausen, S. Recurrent BRCA2 6174delT mutations in Ashkenazi Jewish women affected by breast cancer. *Nat. Genet.* **13**, 126–128 (1996).
33. Oddoux, C. et al. The carrier frequency of the BRCA2 6174delT mutation among Ashkenazi Jewish individuals is approximately 1%. *Nat. Genet.* **14**, 188–190 (1996).
34. Spain, B. H., Larson, C. J., Shihabuddin, L. S., Gage, F. H. & Verma, I. M. Truncated BRCA2 is cytoplasmic: implications for cancer-linked mutations. *Proc. Natl. Acad. Sci.* **96**, 13920–13925 (1999).
35. Jensson, B. O. et al. Actionable genotypes and their association with life span in Iceland. *N. Engl. J. Med.* **389**, 1741–1752 (2023).
36. Mikaelsdottir, E. K., Valgeirsdottir, S., Eyfjord, J. E. & Rafnar, T. The Icelandic founder mutation BRCA2 999del5: analysis of expression. *Breast Cancer Res.* **6**, R284–R290 (2003).
37. Soule, H. D. et al. Isolation and characterization of a spontaneously immortalized human breast epithelial cell line, MCF-10. *Cancer Res.* **50**, 6075–6086 (1990).
38. Bryant, H. E. et al. Specific killing of BRCA2-deficient tumours with inhibitors of poly(ADP-ribose) polymerase. *Nature* **434**, 913–917 (2005).
39. Farmer, H. et al. Targeting the DNA repair defect in BRCA mutant cells as a therapeutic strategy. *Nature* **434**, 917–921 (2005).
40. Vugic, D., Ehlen, A. & Carreira, A. Monitoring homologous recombination activity in human cells. *Methods Mol. Biol.* **2153**, 115–126 (2021).
41. Cong, K. et al. Replication gaps are a key determinant of PARP inhibitor synthetic lethality with BRCA deficiency. *Mol. Cell* **81**, 3128–3144.e7 (2021).
42. Michalet, X. et al. Dynamic molecular combing: stretching the whole human genome for high-resolution studies. *Science* **277**, 1518–1523 (1997).
43. Quinet, A., Carvajal-Maldonado, D., Lemaçon, D. & Vindigni, A. *DNA Fiber Anal. Mind Gap! Methods Enzymol.* **591**, 55–82 (2017).
44. Razavi, P. et al. The genomic landscape of endocrine-resistant advanced breast cancers. *Cancer Cell* **34**, 427–438.e6 (2018).
45. Davies, H. et al. HRDetect is a predictor of BRCA1 and BRCA2 deficiency based on mutational signatures. *Nat. Med.* **23**, 517–525 (2017).
46. Nik-Zainal, S. et al. Landscape of somatic mutations in 560 breast cancer whole-genome sequences. *Nature* **534**, 47–54 (2016).
47. Mendez, M. G., Kojima, S. & Goldman, R. D. Vimentin induces changes in cell shape, motility, and adhesion during the epithelial to mesenchymal transition. *FASEB J.* **24**, 1838–1851 (2010).
48. Gilles, C. et al. Vimentin contributes to human mammary epithelial cell migration. *J. Cell Sci.* **112**, 4615–4625 (1999).
49. Cifone, M. A. & Fidler, I. J. Correlation of patterns of anchorage-independent growth with in vivo behavior of cells from a murine fibrosarcoma. *Proc. Natl. Acad. Sci.* **77**, 1039–1043 (1980).
50. Sachs, N. et al. A living biobank of breast cancer organoids captures disease heterogeneity. *Cell* **172**, 373–386.e10 (2018).
51. Milner, J., Ponder, B., Hughes-Davies, L., Seltmann, M. & Kouzarides, T. Transcriptional activation functions in BRCA2. *Nature* **386**, 772–773 (1997).
52. Edwards, S. L. et al. Resistance to therapy caused by intragenic deletion in BRCA2. *Nature* **451**, 1111–1115 (2008).
53. Sun, L. & Carpenter, G. Epidermal growth factor activation of NF-κB is mediated through IκBα degradation and intracellular free calcium. *Oncogene* **16**, 2095–2102 (1998).
54. Ngo, K. A. et al. Dissecting the regulatory strategies of NF-κB RelA target genes in the inflammatory response reveals differential transactivation logics. *Cell Rep.* **30**, 2758–2775.e6 (2020).
55. Zhong, H., Voll, R. E. & Ghosh, S. Phosphorylation of NF-κB p65 by PKA stimulates transcriptional activity by promoting a novel bivalent interaction with the coactivator CBP/p300. *Mol. Cell* **1**, 661–671 (1998).
56. Kiernan, R. et al. Post-activation turn-off of NF-κB-dependent transcription is regulated by acetylation of p65*. *J. Biol. Chem.* **278**, 2758–2766 (2003).
57. Yang, X.-J., Ogryzko, V. V., Nishikawa, J., Howard, B. H. & Nakatani, Y. A p300/CBP-associated factor that competes with the adenoviral oncoprotein E1A. *Nature* **382**, 319–324 (1996).
58. Xia, B. et al. Control of BRCA2 cellular and clinical functions by a nuclear partner, PALB2. *Mol. Cell* **22**, 719–729 (2006).
59. Le, H. P. et al. DSS1 and ssDNA regulate oligomerization of BRCA2. *Nucleic Acids Res.* **45**, 4507–4516 (2020).
60. Shahid, T. et al. Structure and mechanism of action of the BRCA2 breast cancer tumor suppressor. *Nat. Struct. Mol. Biol.* **21**, 962–968 (2014).
61. Alvaro-Aranda, L. et al. The BRCA2 R2645G variant increases DNA binding and induces hyper-recombination. *Nucleic Acids Res.* gkad1222 https://doi.org/10.1093/nar/gkad1222 (2023).
62. Kim, J. J. et al. PCAF-mediated histone acetylation promotes replication fork degradation by MRE11 and EXO1 in BRCA-deficient cells. *Mol. Cell* **80**, 327–344.e8 (2020).
63. Shimelis, H. et al. BRCA2 Hypomorphic missense variants confer moderate risks of breast cancer. *Cancer Res.* **77**, 2789–2799 (2017).
64. Berger, A. H., Knudson, A. G. & Pandolfi, P. P. A continuum model for tumour suppression. *Nature* **476**, 163–169 (2011).
65. Li, C. M.-C. et al. Brca1 haploinsufficiency promotes early tumor onset and epigenetic alterations in a mouse model of hereditary breast cancer. *Nat. Genet.* 1–13 https://doi.org/10.1038/s41588-024-01958-6 (2024).
66. Michelena, J. et al. Analysis of PARP inhibitor toxicity by multidimensional fluorescence microscopy reveals mechanisms of sensitivity and resistance. *Nat. Commun.* **9**, 2678 (2018).
67. Spegg, V. et al. Phase separation properties of RPA combine high-affinity ssDNA binding with dynamic condensate functions at telomeres. *Nat. Struct. Mol. Biol.* **30**, 451–462 (2023).
68. Zerbino, D. R. & Birney, E. Velvet: algorithms for de novo short read assembly using de Bruijn graphs. *Genome Res.* **18**, 821–829 (2008).
69. Koboldt, D. C. et al. VarScan 2: Somatic mutation and copy number alteration discovery in cancer by exome sequencing. *Genome Res.* **22**, 568–576 (2012).

Acknowledgements

We thank all the members of the Carreira lab for their insightful comments on the manuscript. We thank the CRB of Institut Curie (FR) for making available tissue samples used in this work and gratefully acknowledge the patients who donated. We thank Dr. Sandrine Caputo (Institut Curie, FR) for the clinical information on some of the tumor data presented in Supplementary Data 1. We thank MD Katherine L. Nathanson and MD Susan Domchek (Penn. University) for insightful discussions and for providing LOH status information on some of the c.5946delT tumors in Supplementary Data 1. We thank Miguel Angel Quintela's lab (CNIO, SP) for their help in generating organoids. We also thank Maaike Vreeswijk (Leiden Univ.) for helping find information on tumors through the CIMBA consortium and for insightful comments. We thank Anna P. Sokolenko for providing the LOH analysis of some of the c.5946delT tumors in Supplementary Data 1. We also acknowledge Stéphan Vagner and Sarah Lambert (Institut Curie, FR) for insightful comments on the manuscript. We are grateful to Prof. Kyle M. Miller (University of Texas, US) for the plasmid expressing PCAF-GFP and GFP control vector. We thank Eva Sacristán from the Biocomputational Analysis Core Facility at the Centro de Biología Molecular Severo Ochoa (CBM) (CSIC-UAM) for her help in retrieving LOH information from public databases and her support in this project. We also thank the Advanced Light Microscopy and Flow Cytometry facilities of CBM for their technical support. This work was supported by funding from ICGex (Institut Curie), Gray Foundation Basser Initiative "Innovation Award" (Penn. University), the French Breast Cancer Association Ruban Rose "Avenir Prize", Matmut, the

Worldwide Cancer Research and the Spanish Association for Cancer Research (AECC) grant 22-0222 to A.C. A.M. was supported by a French governmental fellowship and a 4th year PhD Fellowship from the French Medical Research Foundation (FRM). S.R.C. was supported by Agencia Española de Investigación (MCIN/AEI) [PID2020115977RB-I00] and [PID2023-150953NB-I00] grants to A.C. E.I. was supported by the Russian Science Foundation (grant 21-75-30015). M.B. was supported by Göngum Saman. High-throughput sequencing was performed by the ICGex NGS platform of the Institut Curie, supported by the grants ANR-10-EQPX-03 (Equipex) and ANR-10-INBS-09-08 (France Génomique Consortium) from the Agence Nationale de la Recherche ("Investissements d'Avenir" program), by the ITMO-Cancer Aviesan (Plan Cancer III), and by the SiRIC-Curie program (SiRIC Grant INCa-DGOS-465 and INCa-DGOS-Inserm_12554). Data management, quality control, and primary analysis were performed by the Bioinformatics platform of the Institut Curie. The Carreira lab is part of the Conexion-Genoma and Conexion-Cancer CSIC hubs.

Author contributions

A.M. and A.C. conceived the study. A.M., J.G.E., S.R.C., C.M., and J.C.C. performed the experiments with assistance from V.B. M.B. extracted the DNA from some of the tumors under the supervision of S.S. and provided clinical information on tumors. S.K.B. provided LOH status results and clinical information on 999del5 tumors. E.G. performed most of the bioinformatic analysis supervised by N.S. Y.M. performed the mutational signature bioinformatic analysis with the supervision of SNZ. A.G. performed the QIBC experiments under the supervision of M.A. A.P.S. and E.I. performed the LOH analysis and provided the clinical information on some of the 5946delT tumors. S.B. supervised next-generation sequencing analysis. A.V.S. and her group at the CRB provided DNA, RNA, and clinical information on tumors from I. Curie. D.S.L. provided insightful ideas and comments on the project and the manuscript. All authors analyzed the data; A.C. wrote the manuscript with input from all the authors.

Competing interests

The authors declare no competing interests.

Additional information

Supplementary information The online version contains supplementary material available at https://doi.org/10.1038/s41467-025-67209-2.

Correspondence and requests for materials should be addressed to Aura Carreira.

Peer review information *Nature Communications* thanks the anonymous reviewer(s) for their contribution to the peer review of this work. A peer review file is available.